Effect of Fracture Pattern's Geometry on Fluid Flow Behavior in Terms of Areal Sweep Efficiency

Tao Wu

2015

Eidesstattliche Erklärung

Ich erkläre an Eides statt, dass ich diese Arbeit selbständig verfasst, andere als die angegebenen Quellen und Hilfsmittel nicht benutzt und mich auch sonst keiner unerlaubten Hilfsmittel bedient habe.

Affidavit

I declare in lieu of oath, that I wrote this thesis and performed the associated research myself, using only literature cited in this volume.

_____   _____
Datum   Unterschrift

Abstract

Petrophysical properties of both fractures and rock matrix and their geometries in a fracture network determined recovery method in naturally fractured reservoir. Water flooding is a commonly used second recovery method for water-wet naturally fractured reservoir. Fractures take only a few percent of total pore volume in a reservoir, however, their several orders of magnitude higher permeability causes injected water preferentially flow in fractures. This leads to early water breakthrough and consequently lower oil recovery from rock matrix.

In this work, influence of geometry of fracture network on fluid flow is investigated by using discrete fracture matrix (DFM) model and a control volume finite element (FE) reservoir simulator. The governing equations for transport modeling are spatial discretized with node-centered finite element and finite volume method (FEFVM).

Two different km-scaled naturally fractured joints patterns of "Moab" member of Entrada sandstone from outcrops on Salt Vally anticline in Arches National Park (Utah, USA) are selected as two-dimensional reservoir analogs. They are mapped with NURBS curves and discretized by using unstructured meshes.

In order to examine the effect of geometry to the fluid flow, based on stress dependent fracture aperture distribution, two different fracture permeability distributions in each joints pattern are created by a geomechanical model.

In simulations, petrophysical properties of both fractures and adjacent rock matrix are based on field studies in Arches National Park. Fluids are assumed to be incompressible. Two relative permeability models are applied for rock matrix respectively. For fractures, the relative permeability model is treated as linear. Water injection rate and production pressure are constant for all simulation runs.

Simulation results of these idealized models showed that permeability distribution of the better intersected fracture network pattern is more sensitive to the change of fracture orientations relative to far-field global stress. Either the model applied with Brooks-Corey (1964) relevant model or the model with its modified alternative, i.e., the power-law model, resulted in different production predictions and shape of saturation profile.

Power-law relative permeability model predicted earlier water breakthrough time than combined Brooks-Corey and Willie-Gardner model. Reversely, in the model, in which fractures have much higher conductivity than rock matrix, it predicted much later water breakthrough time.

In most of the simulation models, results showed little difference between viscous flow and viscous flow with capillary force. It confirms that in km-scaled model in "Moab" sandstone, instead of capillary fracture matrix transfer, but viscous force is dominant in fluid flow.

Areal sweep efficiencies (E_A) were examined by injecting different volumes of water into models, which have varying viscosity ratios between water and oil. Based on other common correlations, a modified Fassihi correlation between mobility ratio and areal sweep efficiency for the model used in this thesis is also derived. Simulation results showed that injecting water volumes have less effect on E_A for oil having much higher viscosity than that of water and viscosity ratio affects E_A easily than water injection volume.

Kurzfassung

Petrophysikalische Eigenschaften von Klüften und Gesteinsmatrix und die Geometrie der Kluftnetzwerke sind entscheidend für die Gewinnungsmethode einer natürlich geklüfteten Lagerstätte.

Wasserfluten ist eine häufig eingesetzte Sekundär-Gewinnungsmethode in wasserbenetzten natürlich geklüfteten Lagerstätten. Klüfte nehmen nur wenige Prozent des gesamten Porenvolumens einer Lagerstätten ein. Die um mehrere Größenordnungen höhere Permeabilität führt zu einem verfrühten Wasserdurchbruch und damit einer niedrigeren Ölgewinnung aus der Gesteinsmatrix.

In dieser Arbeit wird der Einfluss der Geometrie von Kluftnetzwerken auf das Strömungsverhalten mittels Discrete-Fracture-Matrix-(DFM)-Modelle und eines Finite-Volumen-(FV)-Finite-Elemente-(FE)-Simulators untersucht. Die Basis des Durchflussmodells sind räumlich diskretisierte knotenzentrierte FV-FE-Modelle.

Zwei unterschiedliche KM-skalierte natürlich geklüftete Mustervorlagen des Moab-Teils des Entrada-Sandsteins von Sandsteinfelsen des Salt-Valley-Anticlines im Arches National Park (Utah, USA) wurden zur 2D Analog der Lagerstätten verwendet.

Um die Auswirkung der Geometrie auf das Strömungsverhalten zu untersuchen, wurden basierend auf einer spannungsabhängigen Kluftöffungsverteilung für jede Mustervorlage zwei unterschiedliche Permeabilitätsverteilungen mittels eines geomechanischen Modells erstellt.

Die in den Simulationen verwendeten petrophysikalischen Eigenschaften von Klüften und Gesteinsmatrix basieren auf Feldstudien im Arches National Park. Flüssigkeiten wurden als inkompressible angenommen. Zwei relative Permeabilitätsmodelle wurden für die einzelnen Gesteinsmatrix angewandt. Für Klüfte wurde die relative Permeabilität als linear angenommen. Die Wasserinjektionsrate und der Fördersondendruck sind konstant bei beiden Simulationen.

Die Simulationsergebnisse dieser idealisierten Modelle zeigen dass die Permeabilitätsverteilung des besser durchbrochenen Kluftnetzwerkmusters empfindlicher auf Änderungen der Kluftorientierungen relative zum globalen Spannungszustand reagiert.

Das auf dem Power-Law basierende relative Permeabilitätsmodell sagt einen früheren Wasserdurchbruch als das andere modifizierte Brooks-Corey-Modell und Willie-Gardner-Modell voraus. Umgekehrt wird in dem Modell, in dem die Klüfte eine wesentlich höhere Leitfähigkeit als die Gesteinsmatrix besitzen, ein viel späterer Wasserdurchbruch als im modifizierten Brooks-Corey-Modell prognostiziert.

Mit Ausnahme des Modells mit besser durchbrochenen und besser leitenden Klüften sind in den Simulationsmodellen keine markanten Unterschiede zwischen den Szenarien mit und ohne Kapillarwirkung der viskosen Strömung erkennbar. Es kann gezeigt werden dass statt des kapillaren Kluft-Matrix-Transfers die viskose Kraft das Strömungsverhalten dominiert.

Es wurden Flächendurchlaufwirkungsgrade (engl. Areal Sweep Efficiency) mittels unterschiedlicher eingepresster Wasservolumen in Modellen, die variierende Viskositätsverhältnisse zwischen Wasser und Öl aufweisen, untersucht. Die Simulationsergebnisse zeigen, dass das eingepresste Wasservolumen einen geringen Einfluss auf den Flächendurchlaufwirkungsgrad

der Verdrängung von Öl aufweist, welches eine viel höhere Viskosität als die Verdränger-flüssigkeit besitzt. Korrelationen zwischen Bewegungsverhältnissen und dem Flächendurch-laufwirkungsgrad wurden ebenso abgeleitet.

Acknowledgements

Contents

List of Tables

List of Figures

Chapter 1

Introduction

The presence of fracture can significantly affect the mechanisms of oil and gas recovery from petroleum paths.

Because of the uncertainties of field data, to accurately predict the flow behavior in the naturally fractured reservoir is challenging. In fracture systems, size, orientation and aperture of each fracture alters with its position corresponding to the stress state imposes on it. The characteristic of whole fracture system can not be described by the information collected from single well, such as cores, drill cutting, image logs and well testing data

Besides the accurate description of the naturally fractured reservoir, the numerical model and the simulation methods determine the success of the prediction of oil recovery from such reservoirs. Since 1960s, based on some assumptions, models, such as the early dual continuum model, the later numerical modeling with dual-porosity concept and the present widely used discrete fracture networks (DFN) are developed for the simulation of multi-phase flow in fracture systems. Unlike the DFN model, which considers only the flow in the fractures and meanwhile it requires high accuracy of the description of fracture networks, discrete fracture and matrix model (DFM) considers both the flow in the higher permeable fractures and in the surrounding matrix.

In this thesis, numerical simulations of water flooding are conducted on km-scaled DFM reservoir analog models from naturally fractured outcrops in Arches Nation Park (Utah,USA). The larger size of the model makes it possible to observe the development of the saturation fronts sufficiently. In the reservoir analogs, fractures are well characterized. Many geological surveys have been done in the area. Dyer (1983) recognized the fracture sets in the Garden area, Cruikshank *et.al.* (1991) studied the sequences of the joints in southwest (SW) limb of the anticline, Antonellini and Aydin (1993) studied the petrophysical properties of sandstone in Arches National Park and Lorenz (2001) *et. al.* interpreted several fracture domains in the northeast (NE) limbs of the anticline. Because of its well developed interconnected fracture pattern, this area could be a potential reservoir if it was undergroud structure. Simulation results compare the impacts of the fracture networks' geometries on the fluid flow.

In the following sections, introduction of key issues related to naturally fractured reservoirs and the performance of water flooding in such reservoirs is first presented. Followed by the discussion of the governing equations for the simulation methods and methodology of the simulation model, the geological settings of the chosen outcrops are described. With the

help of a computer-aided design (CAD) program, the fracture traces are mapped and represented with NURBS curves and then geometry structures are discretized on unstructured meshes. The steady-state two-phase pressure-driven simulations are conducted by using a in CSMP++ developed Transport Scheme (Bazrafkan, Matthäi, 2011), which combined the finite element (FE) and finite volume (FV) method. In this discretization technique, the pressure field is computed by using implicit FE-formulations and the saturation transport is computed by using finite volume (FV) algorithms. In the simulation results section, results from different simulation scenarios are presented and analyzed.

Chapter 2

Methodology

2.1 Characteristics of Fractures

2.1.1 Types of Fractures

As shown in Figure 2.1, in mechanics, according to the displacement modes caused by the stress state, fractures are classified into three modes:

Mode I (opening mode): tensile stresses are perpendicular to the crack plane and pull the crack open.

Mode II (sliding mode): shear stresses act parallel to the crack plane and push the upper part of the crack back and pull the lower part of the crack forward. The crack doesn't move out of its plane but slide along itself.

Mode III (tearing mode): shear stresses are not only parallel to the crack plane, but also to the crack front. This causes the crack to move out of its original plane.

Figure 2.2 illustrates the fracture development under the stress condition. Figure 2.3 lists the components of stress tensor. In Figure 2.2, Point "A", "B" and "C" is the touching point of the different Mohr stress circles and Mohr envelope respectively. They represent different failure conditions of the rock. At point "A", the principle maximum compressive stress σ_1
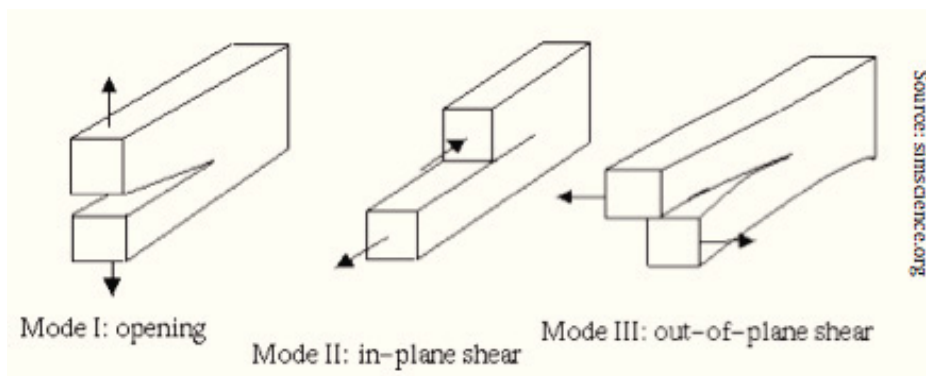
Figure 2.1: Modes of fractures.
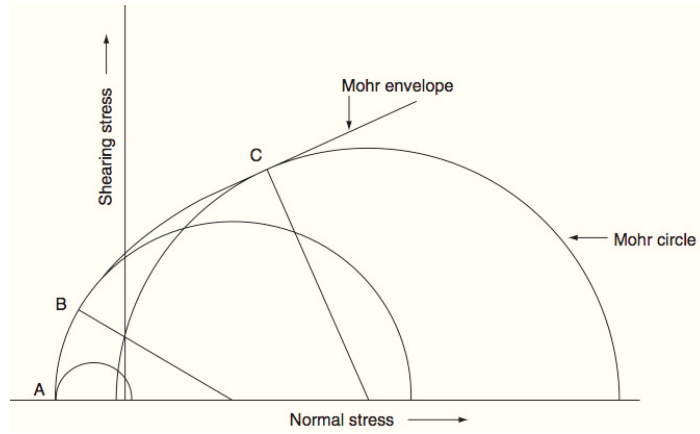
Figure 2.2: Mohr circle[30].
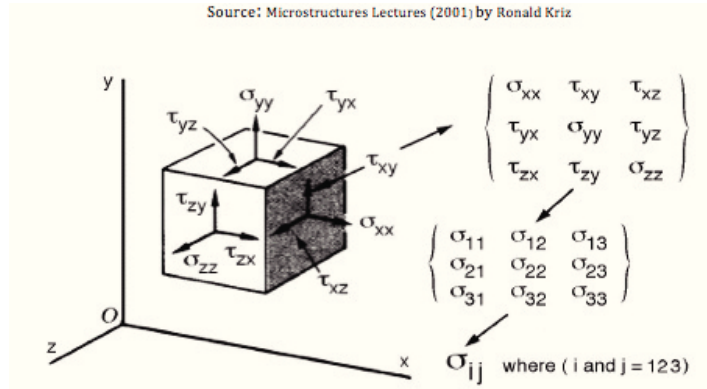
Figure 2.3: Stress tensor components.

is negative and it indicates the opening mode of fractures. In condition "B", maximum compressive stress σ_1 is positive and minimum compressive stress σ_2 is negative. It exhibits both shear and dilational origin. Condition "C" represents the stress condition of shear fractures.

2.1.2   Influences of Fractures on the Recovery of the Reservoir

Fracture characteristics are always correlated with the discrete fracture information, such as: transmissivity, size, orientation, location and spacing. In order to describe the reservoir correctly, the works must include mapping the sizes of the fractures, the connectivity, the conductivity and the frequency distribution. All these information then have to be converted into reliable fractured network characteristic[14]. For large-scale simulation, the average of fracture network characteristic, e.g., conductivity, intensity, anisotropy and storage capacity, are needed.

All processes applied in the unfractured reservoir can still be used in naturally fractured
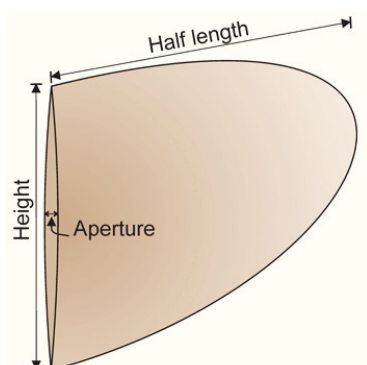
Figure 2.4: Illustration of fracture aperture[26].

reservoir. But, in some circumstances, these two systems have to be treated differently. Like the Gilman[14] mentioned, in the extensively fractured reservoir, not the large viscous force but the capillary and gravity forces dominate. The viscosity ratio still has a pronounced effect on sweep efficiency and the shape of saturation fronts.

In naturally fractured reservoirs, fluid flow is prone to be localized because of the higher permeabilities of the fracture networks than that of the surrounding rock matrix. In the depletion process, fracture network undergoes rapid depletion and provides large surface areas for reservoir fluid in the low-permeability matrix to expand into the fractures. Meanwhile, accompanied by the greater recovery petroleum rates in the naturally fractured reservoir-compared to unfractured reservoir, early water or gas breakthrough are often observed in production wells in naturally fractured reservoir.

On the other hand, fracture flow can lead to free gas flow in the fractures, which, in turn, could invoke gravity drainage of oil from the matrix-leading to very high oil recoveries if the gas-oil gravity drainage process is managed properly.

2.1.3 Specific Parameters of Fractures Used in Simulations of Fluid Flow in Fractured Reservoirs

In addition to parameters, which are needed to be analyzed in conventional simulations, e.g., porosity, permeability, compressibility, wettability, capillary-saturation relations etc., for both matrix and fracture, specific properties of fractures, such as fracture aperture, fracture capillary pressure, fracture relative permeability and shape factor, which describe the characteristics of fractures, must also be known in case of simulation of naturally fractured reservoir.

Fracture Aperture "a":
Aperture of fracture is defined as the perpendicular distance between opposing walls of a fracture[6]. Figure 2.4 shows the illustration of fracture aperture. Fracture aperture depends on fluid pressure and differential stress. Apertures scale with lengths of fractures.

As the fracture aperture matters, we have to consider the influences of the variation of

fracture apertures.

For the small fractures, i.e.,if $R_2 \geq a \geq R_1$ (R_1 refers average pore radius and R_2 is average pore-throat radius),the viscous drag will not be taken into account, meanwhile the capillary pressure controls the distribution of water saturation in the fracture planes[21].

For the large fractures, i.e.,$a \gg R_1$, experiments proved the significance of viscous drag. Capillary pressure gradients are smaller than the production induced gradient. Flow is linear until the velocity in fracture is so fast that inertia effects become important[21].

Fracture Capillary Pressure P_{cf}:

Capillary entry pressure affects strongly the ensemble relative permeability K_r of rock. Based on the Younge-Laplace equation of capillarity:

$$P_c = \gamma \left[\left(\frac{1}{r_1} \right) + \left(\frac{1}{r_2} \right) \right] \tag{2.1}$$

and the research of Firoozabadi and Hauge, de la Porte *et al.* summarized the derived fracture capillary pressure as[10]:

$$P_{cfD} = \frac{b_0 P_c}{\gamma} \tag{2.2}$$

In Equation 2.1 and Equation 2.2, γ is the surface tension, r_1, r_2 are radii of the curvature of the curved interface at any point, P_{cfD} is a dimensionless form of fracture capillary pressure and it is a function of wetting phase saturation, b_0 is the mean fracture half-width.

In the water-oil system, de la Porte *et al.* concluded that capillary pressure in fractures P_{cowf} has little effect on overall results and can be set to zero, but in the gas-oil system, for the narrow fractures (i.e.,$< 100\mu m$),the P_{cogf} must be taken into account.

Fracture Porosity ϕ:

According to Gilman, methods used to calculate fracture porosity[14]:

- In the field, it can be calculated from the estimation the fracture spacing and the width which are from core, image logs, and outcrops. In theory, fracture porosities can also be estimated by using the effective permeability and fracture spacing results from pressure buildup tests.

- For reservoir characterization and flow modeling, due to the requirement of the estimation of fracture porosity at each well location and its distribution in 3-D space, fracture porosity can be estimated from conventional logs by relating the fracture porosity with static information such as flexure, lithology, and other intrinsic and extrinsic rock mechanical characteristics. Based on fracture-scaling fractals in terms of fracture width and/or length, it can also be estimated.

Fracture Relative Permeability k_r:

In general, relative permeability is a key factor for the multi-phase flow behavior because of its control on the magnitude of the total mobility λ_t[5]:

$$\lambda_t = k \left(\frac{k_{rw}}{\mu_w} + \frac{k_{ro}}{\mu_o} \right) \tag{2.3}$$

and the shape of the fractional flow function f_i:

$$f_i = \frac{\frac{k_{ri}}{\mu_i}}{\frac{k_{rw}}{\mu_w} + \frac{k_{ro}}{\mu_o}} \tag{2.4}$$

Like J.J. de la Porte *et al.* demonstrated in their studies[10], the classic straight-line relative permeability theories, which was originally presented by Romm in 1966 and it assumed zero capillary fracture pressure and ignored the effects of fracture surface roughness, could not properly define the naturally fractured reservoir and prediction of the performance of reservoir was not reliable.

The relative permeability of fractures is a function of fracture aperture, surface roughness and flow rate. A variable fracture aperture implies that the non-wetting phase will preferentially occupy the wider fracture segments, and because EPM (equivalent porous medium)permeability scales with the cube of aperture, a nonlinear relative permeability saturation relationship is expected for rough-walled fractures.

Flow structure itself has a significant influence on the relative permeability curves. In vertical fractures, the flow potential has significant effect on relative permeability curves.The flow pattern and non-steady modes are also the affecting factors.

Normally, the relative permeability of the rock matrix using the Brooks and Corey (1964) model with an exponent of 2. This value is frequently applied to highly nonuniform materials, such as limestone.

Brooks and Corey Model:

Brooks and Corey model is based on normalized saturation and *pore-size distribution index,* λ and it gives water and oil relative permeabilities,respectively:

$$k_{rw} = (S_e)^{(2+3\lambda)/\lambda} \tag{2.5}$$

and

$$k_{ro} = (1 - S_e)^2 (1 - S_e^{(2+3\lambda)/\lambda}) \tag{2.6}$$

where, S_e is the effective water saturation, which defines as:

$$S_e = \frac{(S_w - S_{wc})}{(1 - S_{wc})} \tag{2.7}$$

As suggested by Valentine et al. (2002), Brooks-Corey model is also used to the fractures, albeit with an exponent between 0.2 and 1 and lower residual saturation than for the matrix[5].

It was proposed by Rossen and Kumar (1992) that at any simulation, when the ratio between gravitational and capillary forces in the fracture system $H_D < 5$, then the non-straight-line relative permeability in fracture should be used. This corresponds to reservoir

with high fracture density and very narrow fractures, and/or low-density difference and high interfacial tension among the phases[10]. H_D was defined as:

$$H_D = \frac{\triangle \rho g H}{\gamma / b_o},$$ (2.8)

where $\triangle \rho$ is the density difference, g is the gravitational acceleration, H is the fracture height, γ is the interfacial tension and b_o is the mean half fracture aperture.

Shape Factor σ:

Shape factor is a key parameter in determining the fluid transfer between matrix and fracture. This concept was introduced by Barenblatt in 1960[4]. Among the different proposals for the values of shape factor, the Warren-Root and Kazemi shape factors are the most famous[32].

Kazemi *et al.* derived the shape factor by using a first-order finite-difference discretization and obtained a simple form for a 1D single-matrix block:

$$\sigma = \frac{4}{L^2}$$ (2.9)

If the matrix blocks are rectangular prisms with sides L_x L_y L_z, then the shape factor has the form:

$$\sigma = 4 \left(\frac{1}{L_x^2} + \frac{1}{L_y^2} + \frac{1}{L_z^2} \right)$$ (2.10)

Normally, the shape factor must be evaluated as a history-match parameter.

Gilman[14] mentioned that shape factor is a function of fracture spacing. Chang, Lim and Azis demonstrated that shape factor is also a function of time[31]. Van Heel *et al.* stressed that the affecting factors for selection of appropriate shape factor are not only the geometry of matrix block, but also the dominant underlying physical recovery mechanisms.

Combining the value from Kazemi *et al.* (1992) and Zhang *et al.* (1996), for the common expression for shape factor based on water imbibition experiments[14][15]

$$\sigma = \frac{1}{V} \sum_{i=1}^{I} \frac{A_i}{d_i}$$ (2.11)

where,

A_i–disignate exposed fracture surface
i–numbers of given matrix
V–matrix volume
d_i–the distance between the block center and the exposed fracture surface
I–number of exposed fractured plans

A.P.G.van Heel and P.M.Boerrigter summarized different expressions for shape factor in their studies. Meanwhile, they got conclusions that for a given matrix block, convection and diffusion- dominated processes require different shape factors[31]. The importance of selecting the shape factor appropriate for the dominant physical recovery process was confirmed in their simulation results. They recommended to use the steady-state or transient- diffusion- type shape factors for diffusion- dominated processes and the convection-type shape factors for convection-dominated processes.

2.1.4 Cubic Law

Cubic law states the linear relationship between the volumetric flow rate and the cubed aperture in a smooth-walled parallel plate model.

Cubic law was originally deviated from the solution of Navier-Stokes equations in the parallel plate model. The parallel plate model is the simplest model for fluid flow through rock fractures. In this model, the walls of the two parallel plates were assumed smooth and it is the only fracture model which made it possible to calculate the hydraulic conductivity [37].

Since 1868, J. Boussinesq firstly studied the effect of friction on the laminar flow of fluids between the smooth parallel plates[36], researchers like Huitt (1955), Lamb (1957), Snow (1965,1968a,1968b), and Sharp *et al.* (1972), *etc.*[23] have developed the basic equation to model flow in fractures by using paralle plate model.

Witherspoon *et al.* (1980)[34] stated the simplified form of cubic law in their study:

$$\frac{Q}{\triangle h} = C(2b)^3 \tag{2.12}$$

In the case of straight flow, C is given by:

$$C = \left(\frac{w}{l}\right)\left(\frac{\rho g}{12\mu}\right) \tag{2.13}$$

where, Q is the flow rate, $\triangle h$ is the difference in hydraulic head, C is a proportional constant, 2b is the fracture aperture, w is fracture width and l is fracture length.

According to Zimmermann *et al.*(1996)[37], permeability of fracture can be written as:

$$k = \frac{h^2}{12} \tag{2.14}$$

where, h is fracture aperture.

Correspondingly, fracture transmissivity T is obtained by multiplying the permeability and the cross-sectional area of fracture:

$$T = \frac{wh^3}{12} \tag{2.15}$$

The traditional cubic law accurately describes the flow in parallel plate model. Actually, the flow in naturally fractured reservoir is far more complicated than in the simple model, *e.g.,* the fracture walls are not smooth, but rough, and the apertures are not uniform, but vary.

Like Klimczak *et al.*[17] mentioned, the equivalent aperture, which is called hydraulic aperture is now used. The hydraulic aperture is actually smaller than the mechanical aperture. There are also different approaches correlating mechanical to the hydraulic apertures.

2.1.5   Co/Counter-Current Imbibition

Water imbibition is an efficient recovery mechanism for water-wet fractured reservoir because of the capillary contrast between the fracture and the matrix[24]. The capillary pressure causes the water imbibe into the water-wet matrix block and the oil will be displaced into the fractures.

According to the varies of the ratio of gravity to capillary force and the changes of the boundary condition of the matrix block, water imbibition differs from co-current and counter-curent spontaneous imbibition.

In *co-current* imbibition, both oil and water flow in the same direction, water pushes oil out of matrix. It occurs when the block is partially covered by water.

In *counter-current* imbibition, oil and water flow in opposite directions. Counter-current imbibitions active only in model regions where water is in contact with the fracture-matrix interface. It is not an important recovery mechanism in mixed or oil-wet carbonates.

In their experiments, Bourblaux and Kalaydjlan found that counter-current imbibition process has slower oil recovery, slightly lower ultimate oil recovery, and smoother water/oil front comparing with the cocurrent imbibition predominant flow[7]. Pooladi-Darvish and Firoozabadi also proved in their experiments that co-current imbibition led to more efficient recovery [28].

- Mathematical Formulation

  Based on the assumption of incompressible flow and the neglect of gravity, the counter-current imbibition in one-dimension (1D) can be described as[19] :

$$\frac{\partial}{\partial x}(D(S_x)\frac{\partial S_w}{\partial x}) = \frac{\partial S_w}{\partial t} \tag{2.16}$$

  this is a nonlinear diffusion equation and the diffusion coefficient is

$$D(S_w) = -\frac{k}{\phi}\frac{k_{ro}}{\mu_o}f(S_w)\frac{dP_c}{dS_w} \tag{2.17}$$

16

which is a strong function of saturation.

$$f(S_w) = \frac{1}{1 + \frac{k_{ro}}{k_{rw}}\frac{\mu_w}{\mu_o}} \tag{2.18}$$

McWhorter *et.al.*[22] gave the mathematical formulation of cocurrent imbibition includes an additional convective term

$$\frac{\partial}{\partial x}(D(S_x)\frac{\partial S_w}{\partial x} - q_t f(S_w)) = \frac{\partial S_w}{\partial t} \tag{2.19}$$

and the corresponding diffusion coefficient is

$$D(S_w) = -\frac{k}{\phi}\frac{k_{ro}}{\mu_o}\frac{P_c}{dS_w} \tag{2.20}$$

- Numerical Model

  In general, the numerical model is used to study the counter- and cocurrent imbibition in finite-size porous media. By coupling with the continuity equation and the generalized form of Darcy's law for two-phase flow, Peaceman *et. al.* developed:

$$\nabla(k\frac{k_{ro}}{\mu_o}\nabla p_o) = -\phi\frac{dS_w}{dP_c}(\frac{\partial p_o}{\partial t} - \frac{\partial p_w}{\partial t}) \tag{2.21}$$

$$\nabla(k\frac{k_{rw}}{\mu_w}\nabla p_w) = -\phi\frac{dS_w}{dP_c}(\frac{\partial p_o}{\partial t} - \frac{\partial p_w}{\partial t}) \tag{2.22}$$

The initial and boundary conditions are considered for the flow which is purely capillary-driven without effect of viscous force.

2.2 Models to Establish Flow in Naturally Fractured Reservoirs

The models that are commonly used in NFR simulations:

- Dual Porosity Model
- Dual Porosity/Dual Permeability Model
- Discrete Fracture Network (DFN) Model
- Discrete Fracture and Matrix (DFM)Model

Except for DFN model, the other models assume REV (representative pore volume) and use averaging techniques.

2.2.1 Dual Porosity Model Idealization

Dual porosity model is also called sugar-cube model. In this model, fracture and matrix systems are separated into different continua, each with its own set of properties characteristic to the matrix and fracture systems[29].

In this idealization, the REV of the reservoir rock is idealized as matrix blocks with the same sizes, which are separated by interconnected fracture planes. The cubes represent matrix blocks and the spaces between the cubes represent fracture. In this model, there is no matrix-to-matrix flow, but there is matrix-to fracture flow[14]. For this model, one of the most important parameters is apparent matrix size and the transfer function between the matrix and fracture. This model is more suitable for water-wet media than for the mixed-wet system[16].

One limitation of this method is that it cannot be applied to disconnected fractured media and cannot represent the heterogeneity of such a system. Another shortcoming is the complexity in the evaluation of the transfer function between the matrix and the fractures. In fact, in mixed-wet fractured media, a dual-porosity model may lose accuracy due to the effect of gravity[16].

In the numerical simulation of the flow, each individual cube is not treated as discrete grid cell. Fractures are treated as a interconnected continuum and build a flow network with well bore. Normally, viscous displacement from the matrix is ignored.

2.2.2 Dual Porosity/Dual Permeability Model

In contrast to the dual porosity model, in the dual porosity/dual permeability mode, fluid flow occurs not only in matrix-to-fracture but also in matrix-to-matrix.

In the case of multi-phase flow, the significant fluid density differences in the vertical direction will induce gravity drainage in the matrix. The capillary pressure forces, interacts with gravity force will enhance or opposite matrix drainage.

According to Dean *et al.*[11], dual-permeability equation in finite-difference form for fracture is:

$$\Delta[T_{\alpha f}(\Delta p_{\alpha f} - g_{\rho \alpha f}\Delta D)] + T_\alpha(p_{\alpha m} - p_{\alpha f}) + q_{\alpha f} = \frac{V_b}{\Delta t}\delta t\left(\frac{\phi_f S_{\alpha f}}{B_{\alpha f}}\right) \tag{2.23}$$

Dual-permeability equations in finite-difference form for matrix:

$$\Delta[T_{\alpha m}(\Delta p_{\alpha m} - g_{\rho \alpha m}\Delta D)] - T_\alpha(p_{\alpha m} - p_{\alpha f}) = \frac{V_b}{\Delta t}\delta t\left(\frac{\phi_m S_{\alpha m}}{B_{\alpha m}}\right) \tag{2.24}$$

where α denotes for water or oil phase.

These equations are identical to single-porosity equations with additional transfer terms between the matrix and fracture systems. Well terms (q) is not included in the matrix

equation because earlier tests showed that they were insignificant, even when fracture permeabilities are approximately equal to matrix permeabilities. The equations reduce to a dual-porosity formulaiton if the matirx transmissibilities,T_{wm} and $T_{om} = 0$.

The transfer transmissibility involves a geometric shape factor σ. The water transfer transmissibility has the form:

$$T_w = 0.001127\sigma\overline{k}_m \left(\frac{k_{rw}}{B_w\mu_w} \right) \Delta x \Delta y \Delta z \tag{2.25}$$

Where$\overline{k}_m$ is the average matrix permeability and the fluid properties, $k_{rw}B_w\mu_w$ are evaluated upstream. The fluid properties are based on p_{wf} and S_{wf} if water flows into the matrix block, and on p_{wm} and S_{wm} if water flows out of the matrix block.

In *dual permeability* model, equations of single-phase flow:

- *Flow equation in fractures:*

$$\nabla \left(\frac{K_f}{\mu}\nabla P_f \right) - \frac{\sigma K_m}{\mu}(P_f - P_m) + q_f = \phi_f C_{t,f}\frac{\partial P_f}{\partial t} \tag{2.26}$$

- *Flow equation in matrix:*

$$\nabla \left(\frac{K_m}{\mu}\nabla P_m \right) - \frac{\sigma K_m}{\mu}(P_f - P_m) + q_m = \phi_f C_{t,m}\frac{\partial P_m}{\partial t} \tag{2.27}$$

  Both of these two equations are commonly discretized in finite-difference form and are able to compute the pressures of fractures and matrix of all the grid blocks at given time step.

- *fluid in fracture-matrix-transfer in finite difference form, 1-D single-phase flow:*

$$\tau_o = 0.001127\frac{\sigma V K_m K_{ro}}{B_o\mu_0}(P_{om} - P_{of}) \tag{2.28}$$

From the above three equations, it can be seen that shape factor σ, the matrix fluid mobility (i.e., for the oil: $k_m k_o/\mu_o$) and the pressure difference of fracture-matrix affect the matrix-fracture fluid transfer during the depletion processes.

2.2.3 Discrete Fracture Network Flow Modeling

DFN is based on the 3D spatial description of the fractures to build a interconnected fractures' network. Any 3D reservoir rock block is therefor a matrix block.

This model requires very accurate description for fracture network in terms of geometry, conductivity, and connectivity. It is not suitable for field-scaled but intermediate-scaled simulations[14].

In the discrete-fracture model, it is assumed that inside the fractures, all variables remain constant in the lateral direction and the thickness of fracture appears as a factor in front of the 1D integral for the consistency of the integral form[16].

Discrete fracture model is a geometrical simplification of single-porosity model. It is a 1D representation of fractures. Unlike the single-porosity model, it can be applied in large configuration and another difference between the two models is the evaluation of the integral inside the fracture which considerably simplified the problem.

In this model, the fractures are discretized as 1D entities, then this model is implemented using Galerkin finite element method. The main advantage of the finite-element method in reservoir simulation is the possibility to discretize a geometrically complex reservoir with an optimal use of mesh points. The heterogeneity is accounted accurately, and there is no need for the transfer function; it also can be applied to both water-wet and mixed-wet media[16].

For single-phase flow:

- finite element formulation is used to simulate 2D single-phase flow through fractures

- transient transport is solved by upstream finite element method

- fracture and matrix are coupled by using superposition principle

For two-phase flow with capillary pressure:

- use finite volume discretization and use so-called joint-element technique to represent fractures

- based on finite element method and the use of superposition principle to couple the fracture and matrix.

2.2.4 Discrete Fracture and Matrix Model

DFM is one of the stringent ways to study the multiphase flow in naturally fractured reservoir. Unlike the discrete fracture network (DFN) modeling, in DFM model, it considers not only the fluid flow in connected parts of fractures but also the flow occurring in the surrounding rock matrix. The single-continuum approach is used in which both fracture and matrix have discrete representation in the model.The DFM model is discretized using unstructured grid meshes.

Because of the complex of the system geometry, the domain is discretized with finite element (FE) method and then at the node of each finite element mesh finite volume (FV) is created by connecting element barycenteres via the midpoints of associated edges.

There are two possibilities to discretize fractured porous media with FEFV method:

- with volumetric FE for both fracture and matrix. In this case, high aspect ratio is required or to use very fine elements for fractures with small apertures.

- with lower dimensional FE for fracture and volumetric FE for matrix, but this is not suitable for the case of $K_m > K_f$.

An alternative formulation of FEFV method is DFEFV (discontinuity finite-element finite-volume) method, it is for purely advective flow in fractured porous media. The only difference between these two methods is, an extra nodes or degree of freedom are added at the fracture-matrix interfaces and the meshes split along the fracture-matrix interfaces so that the discontinuities in concentration or saturation can evolve rather than being suppressed by nodal averaging of these variables.

In order to solve the equations of DFEFV method, it has to be assumed that across the interfaces the pressure of wetting phase is continuous.

The mass balance in pure advection,

$$\phi \frac{\partial C}{\partial t} + \nabla(v_t C) = q \tag{2.29}$$

and the position of saturation front without considering gravity and capillary pressure are solved by FV approach.

2.3 Simulation of Water Flooding

Along with gravity drainage, waterflooding is one of the two common enhanced ways in naturally fractured reservoir recovery. However, the efficiency of the waterflooding depends on the wettability of the reservoir rock.

The important parameters affecting oil recovery from water imbibition are shape factor, capillary pressure and oil mobility, $kk_r o/\mu_o$.

Specially, oil rate is greater as permeability increases and matrix block size decreases (fracture intensity and shape factor increases). Recovery rate also increases as oil relative permeability increases making it easier for water to imbibe and oil to flow out. High capillary pressure increases rate of oil recovery through increased imbibition force.

2.3.1 Water Flooding Patterns

Proper pattern ensure the maximum contact of the injected water with the hydrocarbon systems.

Generally, the selection of a suitable flooding pattern for the reservoir depends on the number and location of existing wells[1].

Essentially, there are four type of flooding patterns: irregular, regular, peripheral, crestal and basal injection patterns.[1]

Irregular pattern
It is used when the production wells and injection wells are not uniformly located or in case of faulting or the localized variations of of porosity or permeability.
Regular patterns:
Figure 2.5 illustrates the classification of regular flooding patterns.

- Direct Line Drive

(a) Four-spot drive.

(b) Nine-spot drive.

(c) Direct line drive.

(d) Seven-spot drive.

(e) Five-spot drive.
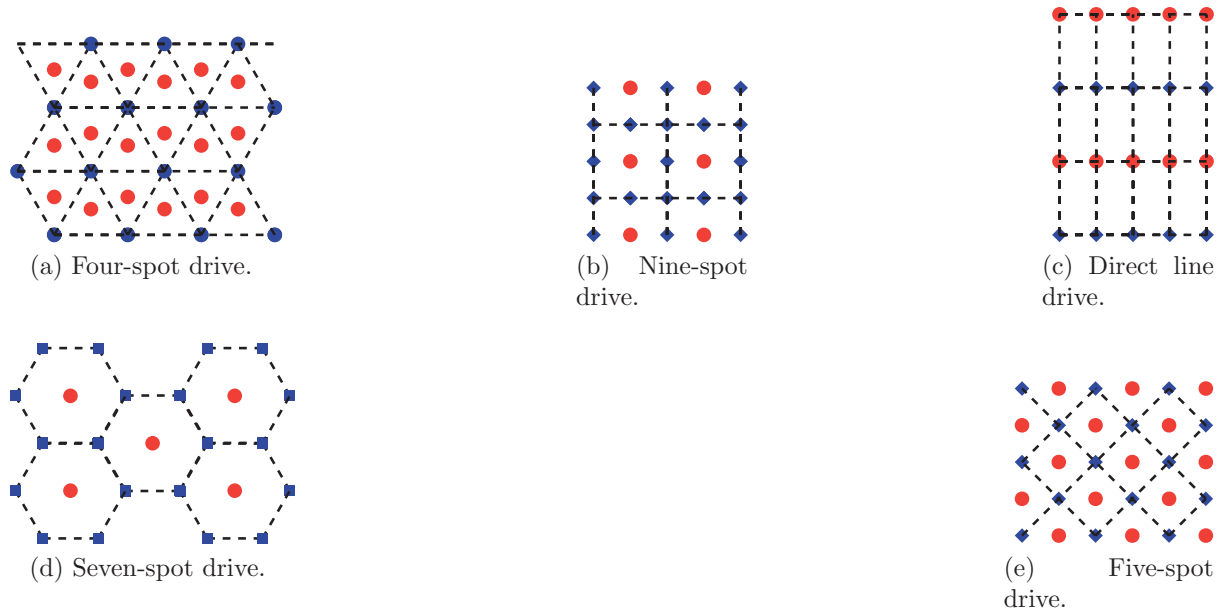
Figure 2.5: Regular Well Patterns.

The lines of injection and production are directly opposed to each other.

– Disadvantages: early water breakthrough if the distances between the injector and producer are small.

• Staggered Line Drive

Unlike the direct line drive, the injector and producers are laterally displaced by a distance of a/2. a is the distance between the wells of the dame type.

• Five-Spot Drive

It is a special case of staggered line drive. The distance between all like wells is constant, i.e., a=2d. d is the distance between lines of injectors and producers. Any four injection wells form a square with a producer well at the center.

• Seven-Spot Drive

The injection wells are located at the corner of hexagon with aproduction well at its center.

• Nine-Spot Drive

This pattern is similar to the five-spot pattern but with an extra injector drilled at the middle of each side of the square.

Crestal and Basal injection pattern

22

Due to the additional benefits being gained from gravity segregation at some dipping reservoir, in basal injection, water is injected at the bottom of the structure.

Peripheral Flooding

In peripheral flooding, injectors are located at the external boundaries of the reservoir and the oil is displaced toward the interior of the reservoir.

2.3.2   Factors Affecting Success of Water Flooding

Water flooding is the most common used method of secondary oil recovery.

Like Thomas, Mahoney, and Winter (1989) pointed out, reservoir geometry, fluid properties, reservoir depth, lithology and rock properties, and fluid saturations are the factors considered when selecting the potential waterflood candidates[1].

- Fluid properties: The viscosity of the crude oil is considered the most important fluid property that affects the degree of success of a waterflooding operation. The oil viscosity has the important effect of determining the mobility ratio that, in turn, controls the sweep efficiency.

- Reservoir Depth:

  In waterflooding operations, there is a critical pressure (approximately 1 psi/ft of depth) that, if this pressure is exceeded, it will permit the injecting water to expand openings along fractures or to create fractures. This results in the channeling of the injected water or the bypassing of large portions of the reservoir matrix. Consequently, an operational pressure gradient of 0.75 psi/ft of depth normally is allowed to provide a sufficient margin of safety to prevent pressure parting[1].

- Lithology and Rock Properties: porosity, permeability, clay content, and net thickness affect flood ability and success.

  In some complex reservoir systems, only a small portion of the porosity, such as fracture porosity, will have sufficient permeability to be effective in water-injection operations. In these cases, a water-injection program will have only a minor impact on the matrix porosity, which might be crystalline, granular, or vugular in nature.

  Caution must be taken, if clay presents in the sand formation, when selecting waterflood candidate. Clay components may clog the pores by swelling and deflocculating.

  Tight reservoir required high water injection pressure, if in the case, the reservoir is thin as well, this might exceed the formation fracture pressure.

- Fluid saturation: Higher oil saturation at the beginning of flood operations increases the oil mobility that, in turn, gives higher recovery efficiency.

2.3.3 Sweep Efficiency

The total displacement efficiency E is the product of the microscopic efficiency E_D and the macroscopic efficiency E_v.

Microscopic Sweep Efficiency

The E_D is the displacement of oil at pore scale. It measures the effectiveness of the displacing fluid to mobilize the oil. It can be calculated by using:

$$E_D = \frac{\overline{S}_w - S_{wirr}}{1 - S_{or} - S_{wirr}} \tag{2.30}$$

Where,

$\overline{S}_w$–average water saturation
S_{wirr}–irreducible water saturation
S_{or}–irreducible oil saturation

Volumetric Sweep Efficiency

The E_v is the measurement of the effectiveness of the displacing fluid areally and vertically sweeping out the reservoir volume.

$$E_v = E_{AS} \times E_{VS} \tag{2.31}$$

The volumetric sweep efficiency is an overall result that depends on the injection pattern selected, off-pattern wells, fractures in the reservoir, position of gas/oil and oil/water contacts, reservoir thickness, permeability and areal and vertical heterogeneity, mobility ratio, density difference between the displacing and the displaced fluid, and flow rate.

- Areal Sweep Efficiency E_{AS} :

  In general, E_{AS} is controlled by well patters, the heterogeneity of reservoir permeability, the mobility ratio and relative importance of gravity and viscous forces.

  In 2D models, the recovery efficiency can be expressed as the product of E_D and E_{AS}:

  $$RE(\%) = E_D \times E_{AS} \tag{2.32}$$

  Areal sweep efficiency can be predicted by using correlations:

  1. Before breakthrough
     The areal sweep efficiency before breakthrough is simply proportional to the volume of the volume of water injected and is given by:

     $$E_A = W_{inj}/[(PV)(S_{wbt} - S_{wi})] \tag{2.33}$$
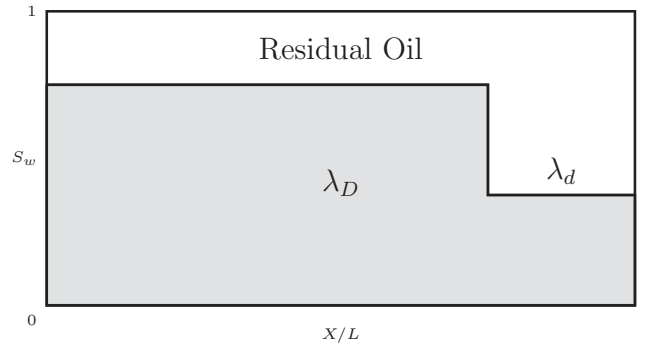
Figure 2.6: Piston Like Displacement.

2. At breakthrough Willhite presented the following mathematical correlation[33]:

$$E_{Abt} = 0.54602036 + 0.03170817/M + 0.30222997/e^M - 0.00509693M \qquad (2.34)$$

where, E_{Abt} =areal sweep efficiency at water break through; M=mobility ratio.

3. After breakthrough

   Craig *et al.* obtained experimental data in horizontal laboratory models representing a quadrant of a five-spot.

   Experimental data for a variety of oil and aqueous systems were correlated empirically[33].

$$E_A = E_{Abt} + 0.633log(W_{inj}/W_{ibt}) \qquad (2.35)$$

   Where, W_{inj} is the volume injected and W_{ibt} is volume injected at breakthrough.

- Vertical Sweep Efficiency E_{VS} :

  Factors, like gravity segregation, mobility ratio, capillary forces and vertical to horizontal permeability variation, have effects on vertical displacement efficiency E_{VS}.

  Dykstra-Parsons model is a simplified model to investigate the reservoir heterogeneity on vertical sweep efficiency. In this model, there is no cross-flow between layers and the gravity was neglected. The flooding was linear at constant pressure drop. Figure 2.6 illustrates the piston-like displacement, which is assumed in Dykstra-Parsons model. As a comparison, Figure 2.7 shows the viscous fingering, which is a development of interfacial instability between displaced and displacing fluid in flow displacement process.

2.4 Governing Equations for Numerical Simulations

General form of mass conservation equation of any fluid with density ρ:

$$\frac{\partial(\rho\phi)}{\partial t} + \bigtriangledown(\rho u) + q_m = 0 \qquad (2.36)$$

25
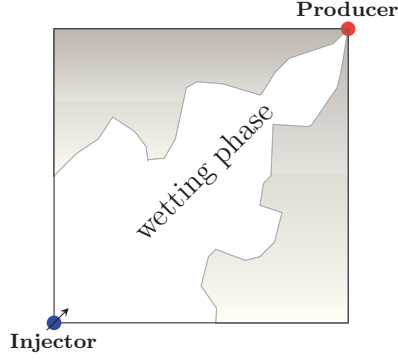
Figure 2.7: Viscous Fingering.

for imcompressible two-phase flow:

$$\begin{cases} \frac{\partial(\rho_w S_w \phi)}{\partial t} + \bigtriangledown(\rho_w u_w) + q_{m,w} = 0, \\ \frac{\partial(\rho_{nw} S_{nw} \phi)}{\partial t} + \bigtriangledown(\rho_{nw} u_{nw}) + q_{m,nw} = 0. \end{cases} \tag{2.37}$$

Navier-stokes equations:

$$\underbrace{\rho\left(\frac{\partial u}{\partial t} + u \bigtriangledown u\right)}_{inertia\,force} + \underbrace{\bigtriangledown p}_{pressure\,force} + \underbrace{\bigtriangledown T}_{viscous\,force} + \underbrace{f}_{external\,force} = 0 \tag{2.38}$$

In most of the reservoir simulators, all the fluids are assumed flowing slow enough, such that the inertia force can be neglected. The equation above can be simplified as:

$$\bigtriangledown p + \bigtriangledown T + f = 0 \tag{2.39}$$

In the simplified navier-stokes equation, T refers to viscous stress tensor. In reservoirs, the variation of the viscous force is assumed as a linear relationship with the flowing velocity. Absolute permeability k is one of the proportional factor.

$$\bigtriangledown T \cong k^{-1} \mu \phi u \tag{2.40}$$

Equation can then be written as:

$$\bigtriangledown p + k^{-1} \mu \phi u + f = 0 \tag{2.41}$$

If only the gravitational force is considered as the external force, then $f = \rho g$, and rearrange the above equation and the *Darcy's Law* is obtained:

$$u = -\frac{k}{\mu\phi}(\bigtriangledown p + \rho g), \tag{2.42}$$

"u" refers to the true fluid velocity, Darcy velocity can be expressed as:

$$u_D = u\phi = -\frac{k}{\mu}(\triangledown p + \rho g) \tag{2.43}$$

Because the simulations are restricted in horizontal plane, the gravitational forces can then be neglected. Darcy's law for fluid phase i can then be simplified to:

$$u_i = -k\frac{k_{ri}}{\mu_i}\triangledown p \tag{2.44}$$

"i" denotes to the wetting or non-wetting-phase.
The total mobility λ_t is defined as:

$$\lambda_t = k\left(\frac{k_{rw}}{\mu_w} + \frac{k_{rnw}}{\mu_{nw}}\right) \tag{2.45}$$

The fractional flow function f for phase i is defined as:

$$f_i = \frac{\frac{k_{ri}}{\mu_i}}{\frac{k_{rw}}{\mu_w} + \frac{k_{rnw}}{\mu_{nw}}} \tag{2.46}$$

The total fluid velocity u_t is the sum of the each phase velocities:

$$u_t = u_w + u_{nw} \tag{2.47}$$

If gravitational and capillary forces are ignored,

$$u_i = f_i u_t \tag{2.48}$$

By using the Equation 2.44, Equation 2.45 and Equation 2.46, u_t can be written as:

$$u_t = \lambda_t \triangledown p \tag{2.49}$$

For the two-phase imcompressible flow, the pressure equation without gravity and capillary pressure is computed as:

$$\frac{\partial p}{\partial t} - \triangledown(\lambda_t \triangledown p) + q_t = 0 \tag{2.50}$$

Assuming incompressibility, conservation of mass implies:

$$\triangledown u_t = q_t \tag{2.51}$$

q_t is a source term.
In two-phase flow, if $S_w + S_{nw=1}$ and $P_c = p_{nw} - p_w$ are taken into the general form of mass conservation equations:

$$\begin{cases} \frac{\partial(\rho_w S_w \phi)}{\partial t} - \triangledown\left(\rho_w \frac{kk_{r,w}}{\mu_w}\left(\triangledown p_{nw} - \frac{\partial P_c}{S_w}\triangledown S_w + \rho_w g\right)\right) + q_{m,w} = 0 \\ \frac{\partial(\rho_w(1-S_w)\phi)}{\partial t} - \triangledown\left(\rho_{nw}\frac{kk_{r,nw}}{\mu_{nw}}\left(\triangledown p_{nw} + \rho_{nw}g\right)\right) + q_{m,nw} = 0 \end{cases} \tag{2.52}$$

By expanding the transient term and dividing both equations by the respective densities, yield:

$$\begin{cases} \frac{1}{\rho_w}\left(S_w\frac{\partial(\rho_w\phi)}{\partial t} + \rho_w\phi\frac{\partial S_w}{\partial t}\right) = 0 \\ \frac{1}{\rho_{nw}}\left((1-S_w)\frac{\partial(\rho_{nw}\phi)}{\partial t} + \rho_{nw}\phi\frac{\partial S_w}{\partial t}\right) = 0 \end{cases} \tag{2.53}$$

By adding the two terms of Equation (2.53), yields:

$$\frac{S_w}{\rho_w}\frac{\partial(\rho_w\phi)}{\partial t} - \frac{1}{\rho_w}\bigtriangledown\left(\rho_w\frac{kk_{r,w}}{\mu_w}\left(\bigtriangledown p_{nw} - \frac{\partial P_c}{S_w}\bigtriangledown S_w + \rho_w g\right)\right) +$$

$$\frac{(1-S_{nw})}{\rho_{nw}}\frac{\partial(\rho_{nw}\phi)}{\partial t} - \frac{1}{\rho_{nw}}\bigtriangledown\left(\rho_{nw}\frac{kk_{r,nw}}{\mu_{nw}}(\bigtriangledown p_{nw} + \rho_{nw}g)\right) + \frac{q_{m,w}}{\rho_w} + \frac{q_{m,nw}}{\rho_{nw}} = 0 \tag{2.54}$$

2.5 Boundary Conditions

In the process of finding solutions, if it is not concerning transient problem, the only necessity is to define the boundary conditions, otherwise, the initial condition has to be defined.

- Types of boundary conditions:

    A. Dirichlet condition: it imposes the value on the boundary.

    B. Neumann condition: it imposes the gradient. E.g., it can be used for defining the influx rate of fluid into a certain domain.

    C. Robin condition: it is also known as impedance boundary and it is a combination of Dirichlet and Neumann conditions.

- Application of each type of boundary condition:

    For the diffusion problem, e.g., $k\frac{\partial^2 p}{\partial x^2}$, at least a Dirichlet condition has to be defined, Neumann condition alone won't result in a stable solution.

    For the transient problem, e.g., $\frac{\partial p}{\partial t}$, both the Dirichlet and Neumann conditions vary with time.

2.6 Solution Method IMPES for Governing Equations

In naturally fractured reservoir, pressure gradients Equation (2.50) on the previous page are solved by linear finite element (FE) method (i.e.,implicit, Galerkin finite element formulation) and the saturations (transport,i.e., extended Buckley-Leverett function) are solved by finite volume method (FVM) (i.e.,explicit, finite volume algorithm).

To obtain the parameters for the simulation, the very first step is to determine $\underline{\underline{K}}_{eff}$. By knowing this, the total mobility λ_t as a function of saturation can be predicted from bulk flow rate in two-phase flow.

To determine $\underline{\underline{K}}_{eff}$, linear Bubnov-Galerkin FE can be used to solve steady-state pressure equation without source term and the Dirichlet boundary condition is assumed. The total flux flowing through the model is measured and to solve

$$\underline{K}_{x(eff)} = \frac{q\mu_w L}{A(P_f(u) - P_f(d))} \tag{2.55}$$

The finite element discretization of the matrix and fracture flow eqations is expressed in terms of nodal oil pressures and water saturations. The standard Galerkin method is employed, wherein the matrix was represented by linear triangular elements and the fractures by line elements.

Equation (2.54) on the facing page is used to compute the p_{nw} and give an initial saturation distribution.

Expanded Equation (2.53) on the preceding page for the non-wetting phase is used to calculate the saturation. Saturation is explicitly evaluated in time and used to solve p_{nw} in the next time step.

When the transient pressure equation is solved with fully implicit finite difference time-stepping approach, the resulting resultants are piece wise linear, this leads to discontinuity across FE faces, therefore node-centered higher-order accurate FVM will be applied to solve transport equation. Because the capillary continuity cannot be assumed in a mesoscale discrete-fracture model,it is treated on the local scale, taking into account local P_c gradients as driving forces for capillary spreading.

In solving the transient-pressure equation, the algebraic multigrid method for system ($SAMG^{TM}$) can be applied, in the case of fixed rate and pressure and no flow through boundary.

Chapter 3

Modeling

3.1 Workflows

- First, the geological structure is represented by NURBS curves.

  Based on the high-resolution satellite image supplied by Google Earth, fracture patterns chosen from the Salt Valley anticline at the Arches National Park are traced with non-uniform rational B-splines (NURBS)-based CAD geometric modeling tool.

  Comparing with polyline curves, NURBS curves are more flexible. Edit of control point affects only the abutting neighbourhood of point, therefore curves can be reshaped. On the other hand, NURBS are differentiable, which smoothly represents shapes as continuous features [25].

- Second, geometry is discretized and the unstructured finite-element meshes are generated.

  Directly on the 2D CAD model, finite element meshes are generated by using ANSYS ICEM CFD. Matrix is discretized with unstructured finite element meshes composed of triangles. Fracture representations are discretized with line elements.

  Parameters, like permeability,relative permeability,saturation and porosity are discretized on the elements. The unstructured grids are used because of their abilities to track free-form geometrical entities and can be generated automatically [25].

- Third, carry out of numerical simulation.

3.2 Geological Model

3.2.1 Geological Settings

Salt Valley anticline locates at Arches National Park in SE Utah (Figure 3.1) and it is a salt-cored asymmetric anticline with sedimentary rocks exposing on its flanks.

The Salt Valley anticline trends NW-SW. It formed over an elongated, evaporate- cored diapiric structure that has a compound history of salt mobility, beginning contemporaneously with or soon after deposition and continuing intermittently through to the present (e.g., Dyer, 1983; Doelling, 1985,1988, 2000; Oviatt, 1988; Cruikshank and Aydin, 1985; Hudec and May, 1998, 1999)[18]
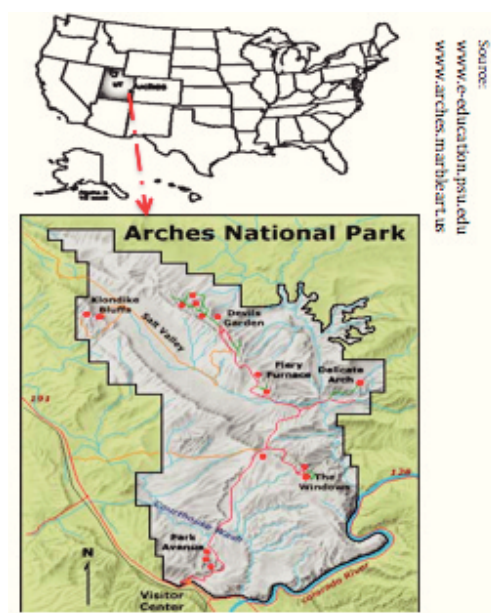
Figure 3.1: Location of Arches National Park.

Because of the lateral movement of underlying ductile strata of salt in the Paradox Formation, local stresses have been changed. It resulted in the development of spectacular multiple or super-imposed kilometer-scale fracture sets on the flanks of the Salt Valley anticline. The fractures occur mainly in the Moab member and Slickrock member (Figure 3.2) of the Jurassic Entrada sandstone (Dyer,1988). Their orientations are related to the states of stresses. In the opening-mode, the fracture propagates in the direction of maximum compression (Pollard and Aydin, 1988)[27]. Due to the aforementioned history of the Salt Valley, the direction of each fracture set does not absolutely correspond to the current structure, but in general, the fractures in the Entrada Sandstone are sub-parallel to the axis of anticline (Lorenz and Cooper, 2001).

Due to the lithology and salt movement, fractures display different spatial distribution and orientation. Lorenz and Cooper distinguished several fracture domains on the NE limb of the anticline. In each of the domains, fracture pattern is well defined and differs from the others. On the SW limb of the anticline, which has been the most studied area, there are four proto-joint domains being defined by Cruikshank and Aydin.

Multiple sets of superimposed fractures create reservoir-quality fracture inter-connectivity within restricted localities of formation.The fracture domains at Salt Valley provide a suite of patterns that may be useful as analogies for similar subsurface reservoirs[18].

3.2.2 Fracture Patterns

In order to compare the influences of different geometries of fracture patterns on the fluid flow in the naturally fractured formation, two fracture patterns from both the NE and SW limbs of the Salt Valley anticline are chosen. One is from in Garden Area, which has a simple fracture network and another one has a better interconnected fracture network.
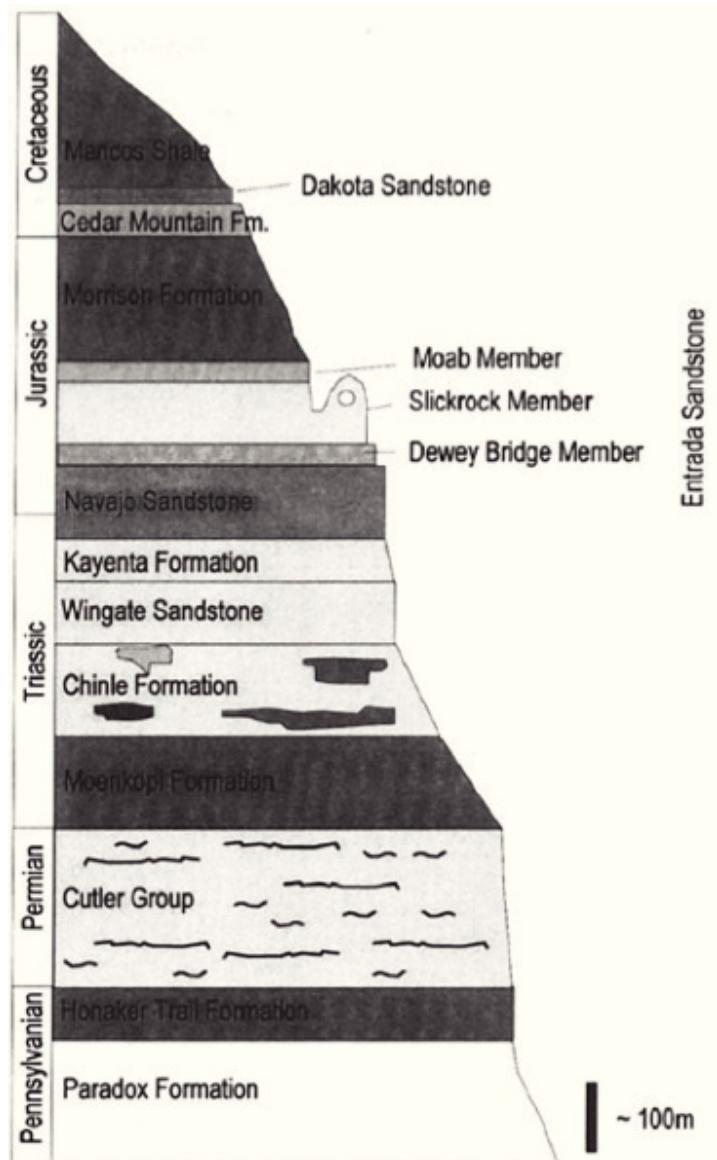
Figure 3.2: Stratigraphic section of Arches National Park (Phillips,1989).
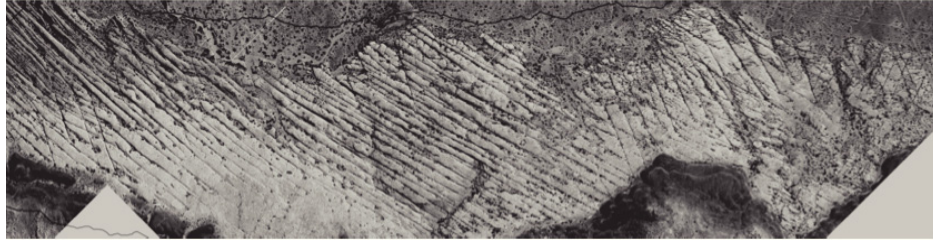
Figure 3.3: Fracture pattern in Garden area.
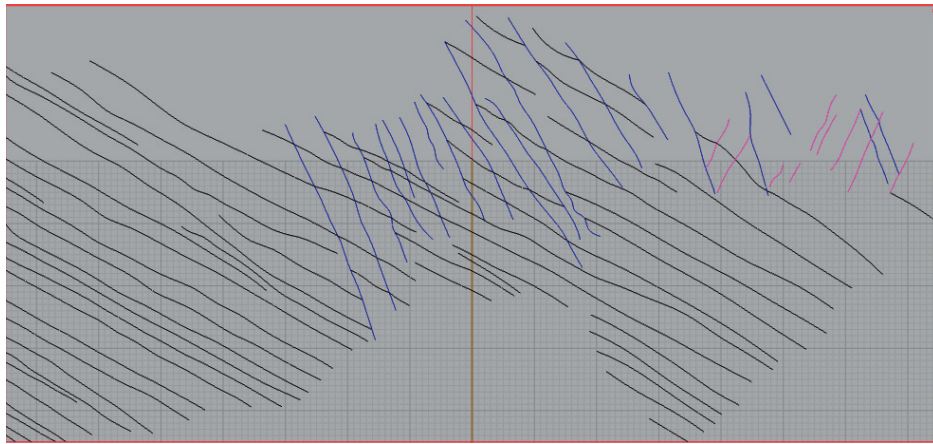
Figure 3.4: Fracture traces in Garden area (original).

Fracture Pattern 1

The fracture pattern 1 (Figure 3.3) is selected in the Garden Area, in which the sequences of fracturing are easily recognizable. Dyer(1983) firstly recognized three different fracture sets in this area. The oldest fracture set in this area occur in the south of this area. They are band faults and the fractures trend roughly N60°E. The second fracture set has a strike of N30°E and it occurs both in the northern and the southern part of this area. They are jointed faults as well. Both of these two fracture sets are deformed because of the mode II and mode III shearing and opened in mode I deformation. The third fracture set is filled throughout the whole area and has a strike of N10°W[35].

Figure 3.4 shows the fracture network in pattern 1, which was traced with the help of NURBS curves. Fracture aperture distribution for this network is shown in Figure 3.5.

Fracture Pattern 2

According to Lorenz and Cooper, two non-coaxial salt-cored anticlines formed nearly at the same time in this area. The southern part of the Salt Valley anticline initiated as a separate structure, which deviated to the southeast of the main structure, during the formation of the present structure the two anticlines coalesced together. This explained the superimposition of fractures in this area (Figure 3.6).

The flow and uplift of the salt strata flexed the overlying formation strata and consequently
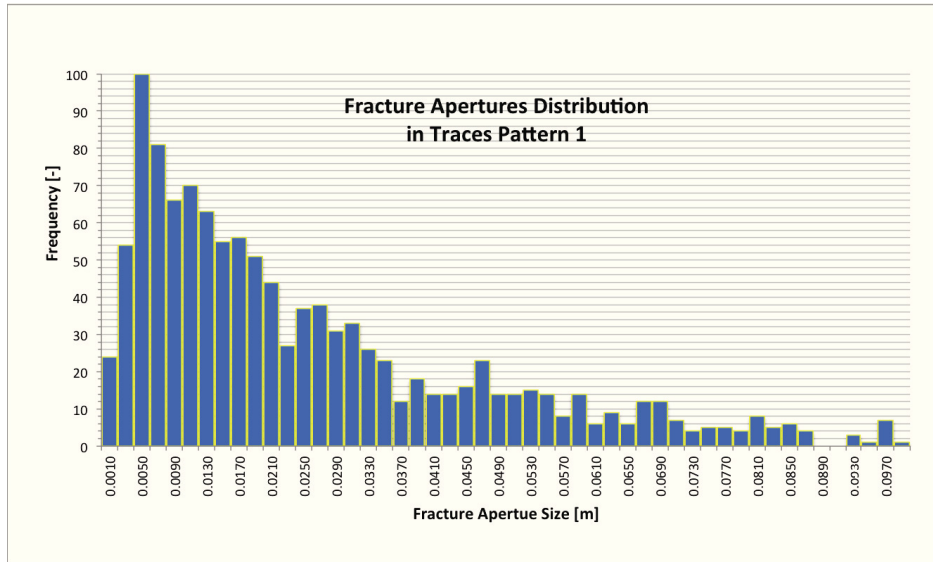
Figure 3.5: Fracture aperture distribution in Garden area.
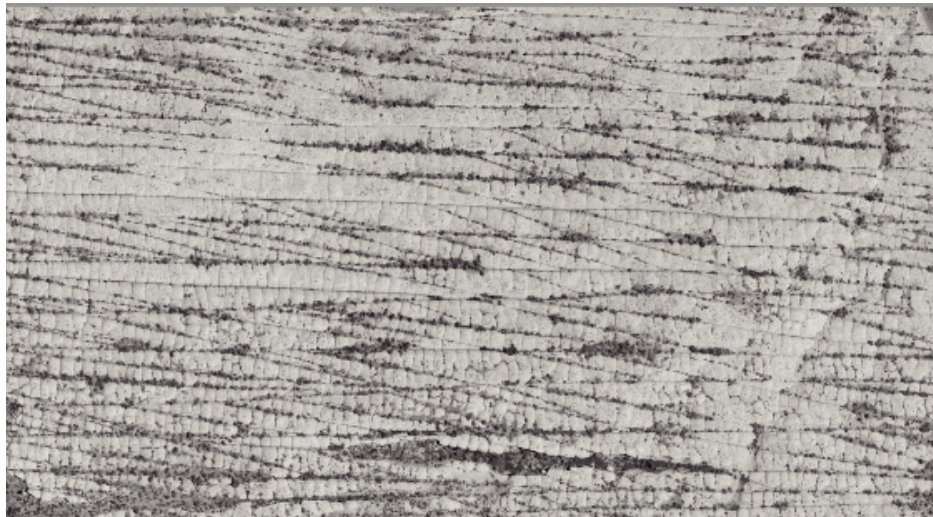
Figure 3.6: Fracture pattern 2.
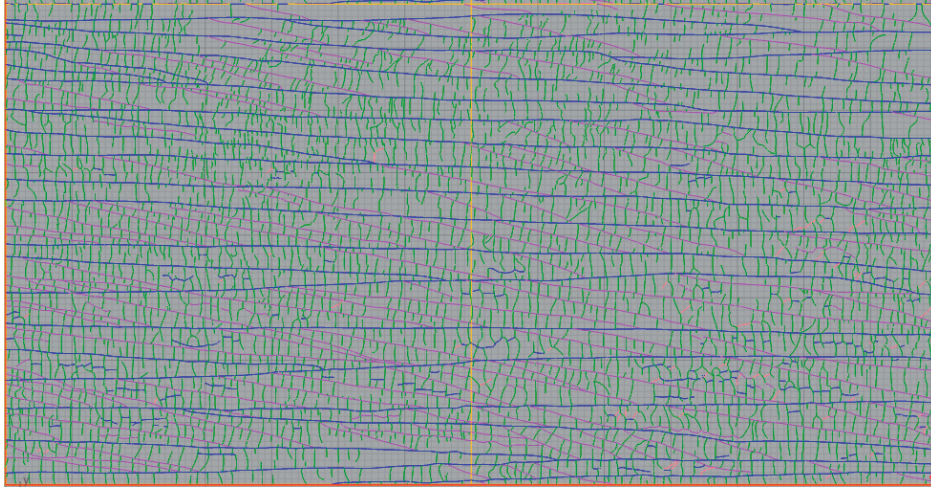
Figure 3.7: Fracture traces of pattern 2 (original).

the fracture set 1 as an extension fracture were formed, trending parallel to the axis of the arching strata. As the fracture set 1 propagated southward, the flank of the anticline became flatter and the different oriented stresses changed the direction of the fractures. The fracture set 2 is such kind of fan-wise extension and it is normal to the axis of the plunging anticline.

According to Dyer's (1983,1988) study, the zoned nature is characteristic of both plan and cross-section views of the joints[35].

The fracture traces in pattern 2 are shown in Figure 3.7 and the two fracture aperture distributions for this network which is under two different stress states respectively are shown in Figure 3.8 and Figure 3.9.

3.3 Petrophysical Properties of Rock Matrix

All the petrophysical properties of the rocks are coming from the studies of Antonellini and Aydin. In their studies of the fault zones in porous sandstones in the area of Arches National Park, they quantified the microstructural and petrophysical properties of the deformation bands and host rocks.

3.3.1 Rock Porosity

By using Video-image analysis and point counting of thin section, rock porosity of the Moab member of the Entrada Sandstone was found to be extremely variable. It ranges from 4% to 28%. From the available samples, 56% of them are between 20% and 30%. Therefor, for the convenience, the average porosity for the simulation is assumed to be 20%[3].
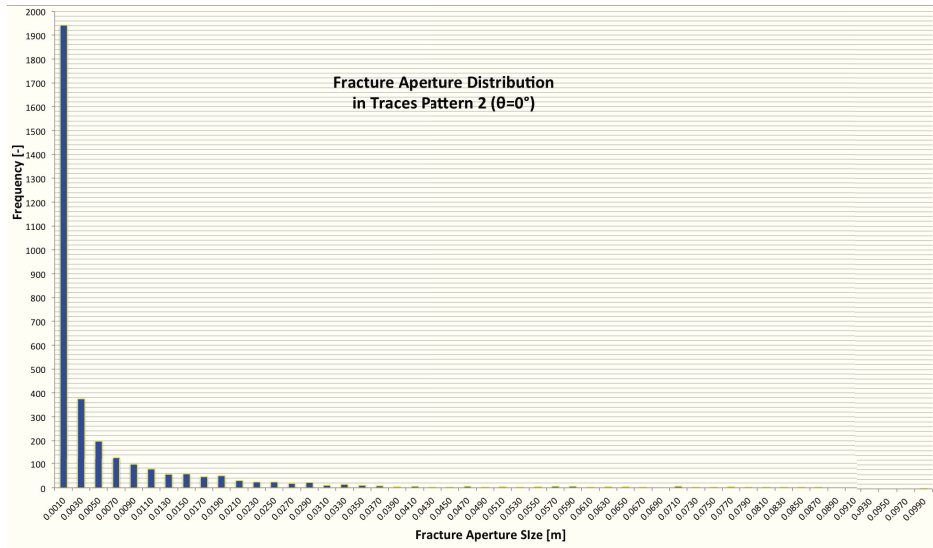
Figure 3.8: Fracture aperture distribution of pattern 2 ($\theta = 0°$).
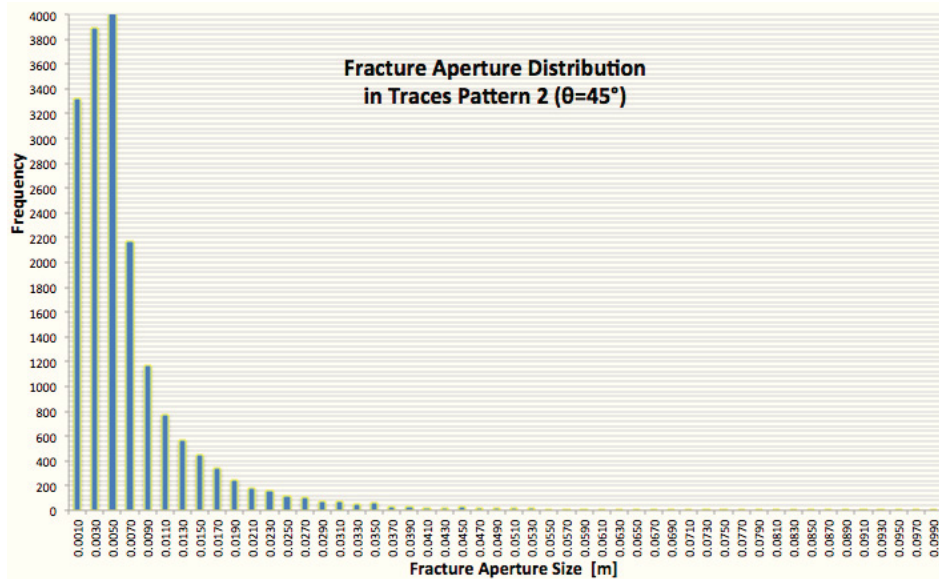
Figure 3.9: Fracture aperture distribution of pattern 2 ($\theta = 45°$).

3.3.2 Rock Permeability

The measurements of rock permeabilites were done by gas injection. Approximately 600 samples were analysed by Antonellini and Aydin and they found that the permeabilites of Moab member of the Entrada Sandstones vary from hundreds of millidarcy to nearly ten thousands of millidarcy. In the simulations, not the extreme values but the moderate value of 700 millidarcy for the rock matrix is used.

3.3.3 Rock Capillary Pressure

Purcell (Purcell, 1949) first found the relationship between the capillary pressure and the interfacial tension, wettability and interconnected pore space.

$$P_c = \frac{2\gamma cos\theta}{R} \qquad (3.1)$$

, where γ is interfacial tension, θ is the contact angle of the wetting phase and R is the interconnected pore space.

Hubbert (Hubbert, 1953) presented the same relation for the expression of capillary pressure:

$$P_c = \frac{C\gamma cos\theta}{d} \qquad (3.2)$$

Instead of the constant coefficient 2 in Equation (3.1), Hubbert expressed it as a dimensionless factor of proportionality C. Parameter d refers to the average grain diameter.

Antonellini and Aydin used Image analysis and obtained the interconnected pore space of the rock matrix in the region of the Arches National Park. They obtaind the minimum width of the pore space resolvable is about 0.0026-0.5 mm.

By using a typical value for hydrocarbon of 25 dynes/cm for the expression of $\gamma cos\theta$ and the the Equation (3.1), they obtained the upper limit of the capillary pressure is 1.66×10^5 Pa. In a similar way, the lower limit of capillary pressure might be inferred as 100 Pa.

3.4 Properties of Fractures

3.4.1 Fracture Aperture

Cruikshank *et.al.* used fracture mechanics to interpret the conditons of the form of the minor fractures associated with joints and faulted joints in the Entrada Sandstone in Arches National Park[9].

They derived Moab Rule of opening width of joints, which provides a lower-bound estimate of the amount of mode I opening.

At the time the joint formed, the width, W, of the joint an only position x* (in this case, y-coordinate is normal to crack and the x* is parallel to x-coordinate) along the x-coordinate is given by:

$$W = 2(\sigma_{yy} + p) \left(\frac{1 - \nu}{\mu} \right) \sqrt{a^2 - x^{*2}}. \qquad (3.3)$$

σ is far-field stress, p is fluid pressure in the crack, ν is Poisson's ratio, μ is shear modulus and a is half crack length.

At the time the joint propagated to its final length a, the width, W_i is

$$W_i = \frac{2K_{IC}}{\sqrt{\pi a}} \left(\frac{1-\nu}{\mu}\right) \sqrt{a^2 - x^{*2}} \tag{3.4}$$

in which, the K_{IC} is the critical value of stress-intensity factor.

For isolated, straight crack subjected to uniform tractions and far-field stresses σ_{yy} and σ_{xy}, the stress-intensity factor is defined:

$$k_I = (\sigma_{yy} + p)\sqrt{\pi a} \tag{3.5a}$$

$$k_{II} = \sigma_{xy}\sqrt{\pi a} \tag{3.5b}$$

Therefore,

$$\frac{k_{II}}{k_I} = \frac{\sigma_{xy}}{(\sigma_{yy} + p)} \tag{3.6}$$

Meanwhile, the amound of displacement, U, across the faulted joint is

$$U = 2\sigma_{xy} \left(\frac{1-\nu}{\mu}\right) \sqrt{a^2 - x^{*2}} \tag{3.7}$$

From the equation above, regardless of the position, x* , along the fracture, the ratio of displacements along a faulted joint can be obtained from the ratio of stresses, if it is known:

$$\frac{U}{W} = \frac{k_{II}}{k_I} = \frac{\sigma_{xy}}{(\sigma_{yy} + p)} \tag{3.8}$$

According to Cruikshank *et al.*, the opening width of a joint at the time the joint formed in mode I loading was greater than or roughly equal to the amount of slip across the faulted joint at the time it kinked in response to mode II loading. Based on the observation of the kink angle and the relationship between the angle and the stress-intensity factor ratio on parent crack, they could estimate the width of the joint at the time it formed. The joint had at least 4 mm of width at the time it formed in mode I and even in some places it could be up to 3 cm.

3.4.2 Fracture Permeability

Fracture permeabilties used for the simulations are calculated with the expression of Zimmermann *et al.* (1996). If fracture aperture is known, its permeability can then be obtained from the relation:

$$k = \frac{h^2}{12}. \tag{3.9}$$

Table 3.1: Petrophysical properties of the matrix rock

Model Domain		Rock Matrix
Material Properties	Units	
Permeability	m^2	7.e-13
Porosity	X	0.2
Relative Permeability Model	BrooksCorey	$\lambda=2$
Entry Pressure	Pa	2000
Residual Water Saturation	X	0.1
Residual Oil Saturation	X	0.1
Fluid Properties		
Viscosity Oil	Pa.s	3.0e-3
Viscosity Water	Pa.s	1.0e-3
Density Oil	kg m^{-3}	850
Density Water	kg m^{-3}	1000
Initial Values		
Saturation Water	X	0.1
Saturation Oil	X	0.9

3.4.3 Fracture Porosity

Fracture porosity is the ratio between the fracture volume and the total bulk volume. For this 2D model, fracture porosity of individual fracture set :

Fracture Porosity=(Fracture Aperture × Total Fracture Length)/Model Size

Properties for the rock matrix and fracture sets are summarized in Table 3.1, Table 3.2 and Table 3.3.

3.5 Numerical Model

A Transport Scheme developed in CSMP++ by Bazrafkan and Matthäi (2011) is used for all the simulations.

The governing equations for transport modeling are spatial discretized with node-centered FE-FVM. The pressure field is computed by using implicit Galerkin FE-formulation on the FE-nodes and the saturation transport is computed with an explicit, i.e., backward in time finite-volume algorithm that is 2nd-order accurate in space.

3.5.1 Simulation Setup

In the nature, it is difficult to obtain km-scaled well developed fracture network pattern, which is in square shape. In order to observe the saturation front development and to conduct the water-flooding by using five-spot pattern, based on the original fracture patterns, models of fracture pattern 1 and fracture pattern 2 are simply doubled from the original rectangles to geometries with

Table 3.2: Material properties of fractures in pattern 1

Model Domain		Fracture Set 1	Fracture Set 2	Fracture Set 3
X-dimension 1400	m			
Y-dimension 1500	m			
Material Properties	Units			
Permeability	m^2	*proportion*	*to the power*	*of the aperture*
Porosity	X	*depends on fracture*	*aperture and total fracture*	*length*
Aperture	m	*power*	*law*	*distribution*
Total fracture length	m	1575.05	9273.19	35321.69
Relative Permeability Model		linear	linear	linear
Entry Capillary Pressure	Pa	0	0	0
Residual Water Saturation	X	0	0	0
Residual Oil Saturation	X	0	0	0

Table 3.3: Material properties of fractures in pattern 2

Model Domain		Fracture Set 1	Fracture Set 2	Fracture Set 3	Fracture Set 4
X-dimension 1400	m				
Y-dimension 1538.8	m				
Material Properties	Units				
Permeability	m^2	*proportion*	*to the power*	*of the*	*aperture*
Porosity	X	*depends on fracture*	*aperture and total fracture*		*length*
Aperture	m	*power*	*law*	*distribution*	
Total fracture length	m	60314	52516	128332	1681
Relative Permeability Model		linear	linear	linear	linear
Entry Capillary Pressure	Pa	0	0	0	0
Residual Water Saturation	X	0	0	0	0
Residual Oil Saturation	X	0	0	0	0

Table 3.4: Stresses applied to the model

Initial arbitrary aperture	m	2.0e-005
Maximum stress	Pa	1.565e+007
Minimum stress	Pa	1.015e+007
Fluid pressure	Pa	1.2e+007

approximately cube-shaped bounding domains. The sizes of final models are 1400m*1500m for fracture pattern 1 and 1400m*1538m for fracture pattern 2 respectively. Although, the mesh size of model has effect on the accuracy of simulation results, but considering the size of the model and the duration of simulation runs, the geological models are not discretized in finer meshes. In fracture pattern 1, 236 fracture traces are discretized into line-elements and rock matrix is discretized into 7284 triangulars. In fracture pattern 2, 8718 fracture traces are discretized into line-elements and rock matrix is discretized into 90668 triangulars.

In all the water-flooding simulation runs, a quarter of five-spot pattern was used. An injector was set on the top left edge of the model and a producer was set at the opposing edge of the cube-shaped km-scale reservoir model. Boundary conditions are set at the injector and producer. In the first part of simulations, at the injector, constant water injection rate of 0.01366 m^3/s corresponding to 0.02 pore volume per year was set and for the producer, the pressure was kept constant for all the simulation runs. Across the model boundaries, there is no flow.

In the second part of simulation, various injection rates and viscosity ratios between water and oil are set to selected model.

The fluid in the simulations is assumed to be incompressible, the density and viscosity of the fluid keep constant all the time, the fluid flow is assumed to be steady-state flow and the gravitational pressure is ignored.

Based on the studies of Cruikshank (1991) and an assumed stress state, fracture aperture distribution is generated from a geomechanical model, whereas the permeability distribution is computed with parallel plate law (Equation (3.9) on page 33). The imposed far-field stresses on the models are assumed to be either normal to the model or at the angle of 45 degree to the model. The applied stresses are listed in Table 3.4 and Figure 3.10, 3.11, 3.12, 3.13 present the permeability distribution of pattern 1 and pattern 2.

For rock matrix, two relative permeability models are applied respectively for both fracture pattern 1 and fracture pattern 2.

In order to include the capillary pressure, which is proven to be the fundamental characteristics of the formation, the first relative permeability model is combined with Brooks-Corey (1964) for predicting water relative permeability K_{rw} and Wyllie and Gardner (1958) correlation for predicting oil relative permeability K_{ro}.

$$K_{rw} = K_{rw,max} S_e^{\frac{2+3\lambda}{2}} \tag{3.10}$$

In all the simulation runs, $K_{rw,max}$ is set to be 0.5.

From capillary pressure data, Willie and Gardner (1958) developed :

$$K_{ro} = \left(\frac{1-S_w}{1-S_{wc}}\right)^2 \frac{\int_{S_w}^1 dS_w/P_c^2}{\int_{S_{wc}}^1 dS_w/(P_c)^2} \tag{3.11}$$
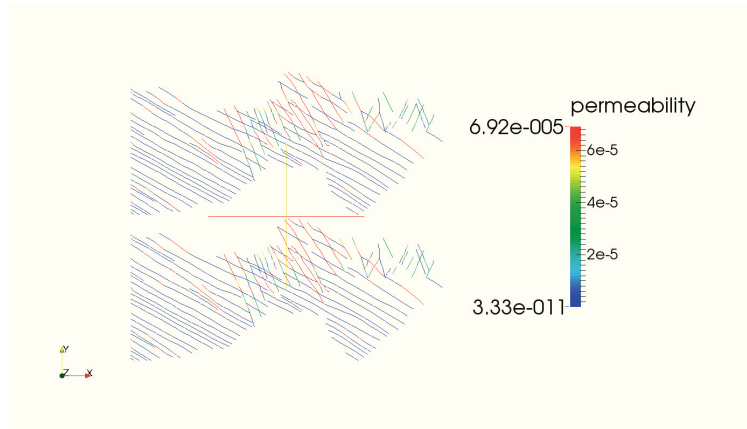
Figure 3.10: Permeability distribution in fracture pattern 1 after model size doubled ($\theta = 0°$).
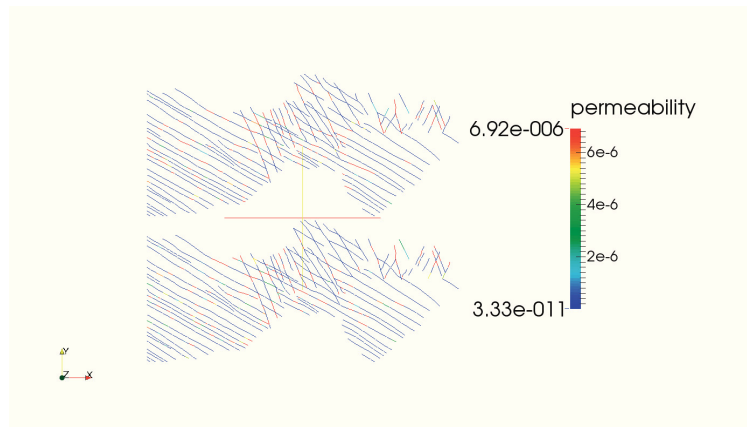
Figure 3.11: Permeability distribution in fracture pattern 1 after model size doubled ($\theta = 45°$).
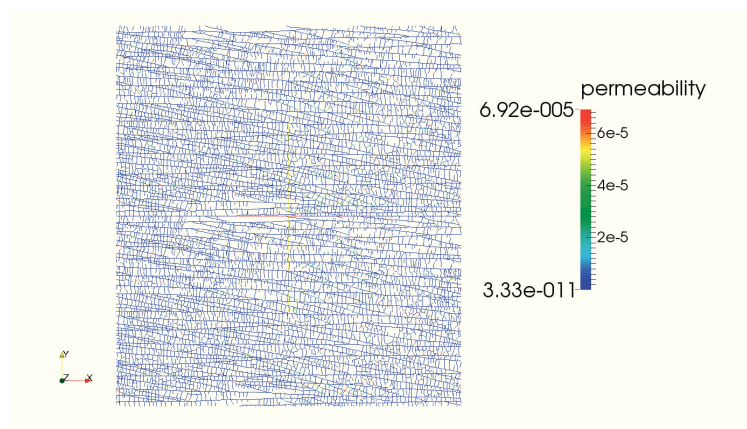
Figure 3.12: Permeability distribution in fracture pattern 2 after model size doubled ($\theta = 0°$).
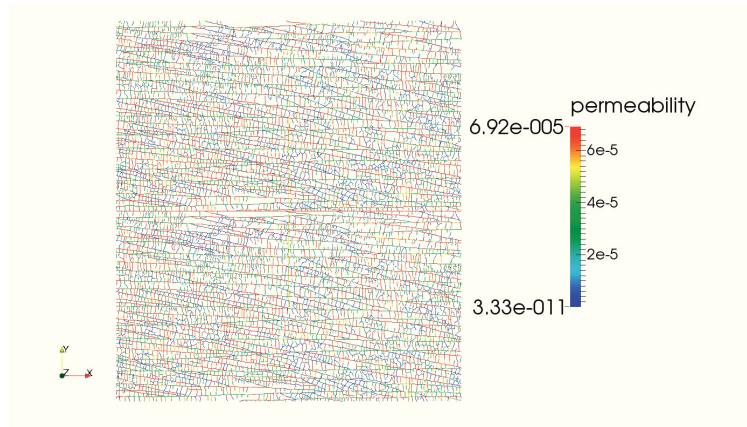
Figure 3.13: Permeability distribution in fracture pattern 2 after model size doubled ($\theta = 45°$).
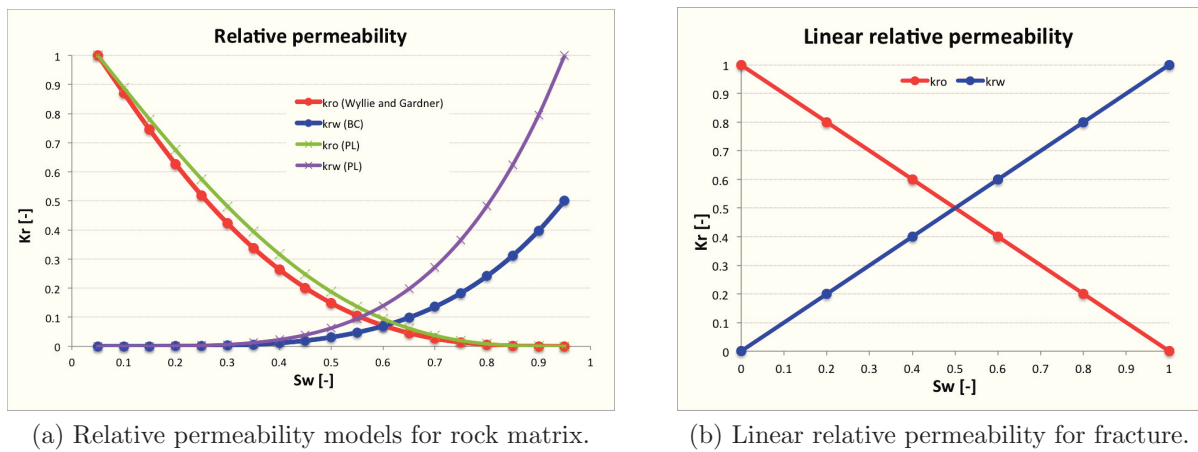
(a) Relative permeability models for rock matrix.

(b) Linear relative permeability for fracture.

Figure 3.14: Relative permeability models applied in models.

As comparison, power-law model is applied as second relative permeability model for rock matrix. It refers to a modified Brooks-Corey relation.

For fracture, linear relationship is used for its relative permeability model.

Chapter 4

Results and Analyses

4.1 Flow Behaviors of Fracture Patterns under Different Stress States

Simulation results showed the difference of relative permeability model to the flow behavior within a same fracture network pattern having different permeability distribution and the effect of fracture-matrix transfer on the fluid flow.

4.1.1 Flow Behaviors in Fracture Pattern 1 Subjected to Stress with $0°$ Orientation

From Figure 4.1, which illustrates the saturation patterns at water breakthrough, different extent of viscous fingering was observed. The power law relative permeability model predicted earlier water breakthrough. With the same simulation setups, in the power law model water cut showed up after 140 days of oil production, meanwhile for the model combined with Brooks-Corey and Willie-Gardner K_r model, water breakthrough occurred on day 164. From both of the two combined K_r models, one is only viscous flow considered and another is considered with viscous flow and capillary force, results showed not too much different on the water breakthrough time, however the model with capillary force predicted more oil production, even though roughly 6.5% more oil was coming from fractures in that viscous flow model.

4.1.2 Flow Behaviors in Fracture Pattern 1 Subjected to Stress with $45°$ Orientation

Like aforementioned, Cruikshank *et.al.* derived the relationship between fracture opening width and their position to the imposed stresses. Changing stress states resulted in the changes of fracture opening width. As the stress oriented from 0 degree to 45 degree, the opening width of fracture changed correspondingly. Figure 3.10 and 3.11 illustrate different permeability distribution of the models having the same fracture network patterns. In the model with 0° orientation of stress, the N30°E fracture set is much more permeable than other fracture sets and adjacent rock matrix, fluid flow is therefore focused along the more conductive fractures. In the model with 45° orientation
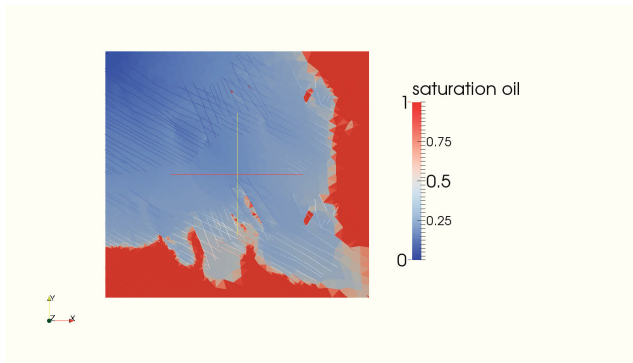
(a) Saturation profile of viscous flow using combined Brooks-Corey and Willie-Gardner relative permeability model.
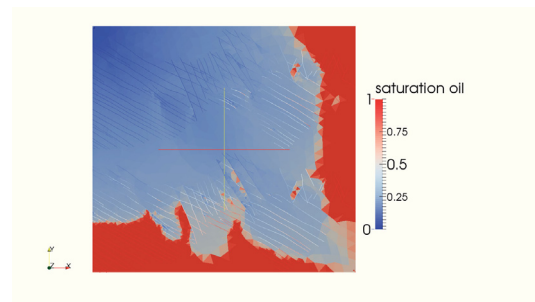
(b) Saturation profile of viscous flow with capillary force (Brooks-Corey and Willie-Gardner).
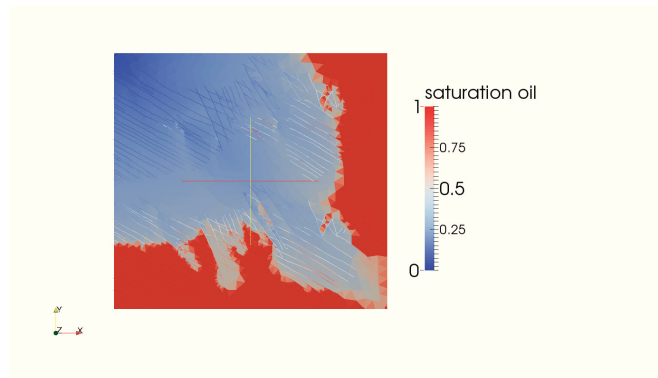
(c) Saturation profile of viscous flow using power law relative permeability model.

Figure 4.1: Saturation profiles at water breakthrough (pattern 1, $\theta = 0°$).
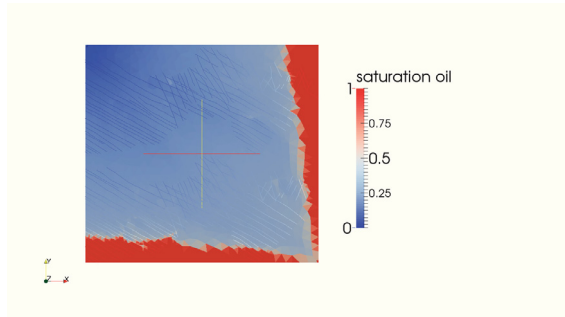
(a) Saturation profile of viscous flow using combined Brooks-Corey and Willie-Gardner relative permeability model.

(b) Saturation profile of viscous flow with capillary force (Brooks-Corey and Willie-Gardner).

(c) Saturation profile of viscous flow using power law relative permeability model.

Figure 4.2: Saturation profiles at water breakthrough (pattern 1, $\theta = 45°$).

of stress, there is no extreme permeable fracture among all the fractures, the driven of fluids was relatively uniform and the viscous fingering was not obvious (Figure 4.2).

Figure 4.3 compared the average oil saturations and fluid pressures along the flow paths in the two models exposed to different far-field stresses at water breakthrough. Figure 4.4 showed velocity magnitudes of the flows at water breakthrough of that two models.

According to the simulation results, roughly 15% more oil could be produced from less viscous fingering affected model. Table 4.1 lists the oil productions from the idealized models.

Figure 4.5 and Figure 4.6 plot the average oil saturations and the fluid pressures along the horizontal distance from injector to producer respectively. The plots showed the comparisons of simulation results of scenarios: viscous flow, viscous flow with capillary force and viscous flow with capillary force using power law relative permeability model.
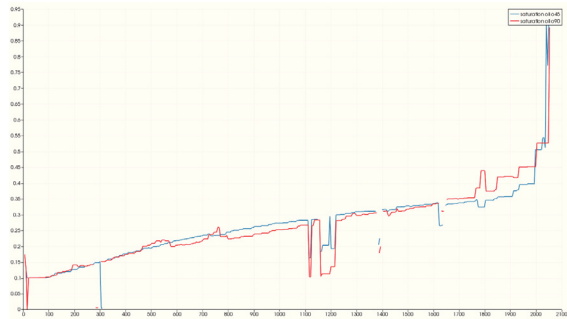
(a) Comparison of average oil saturations along the flow paths.
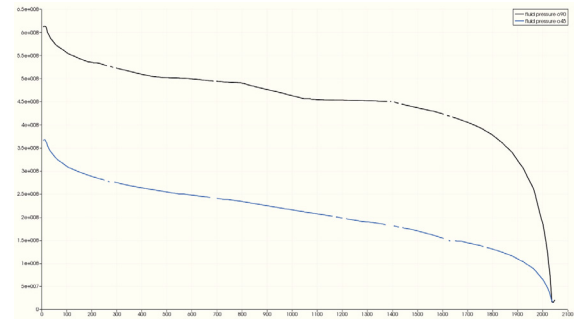
(b) Comparison of fluid pressures along the flow paths.

Figure 4.3: Average oil saturations and fluid pressures of viscous flow models exposed to two stress states ($\theta = 0°$,$\theta = 45°$) at water breakthrough.
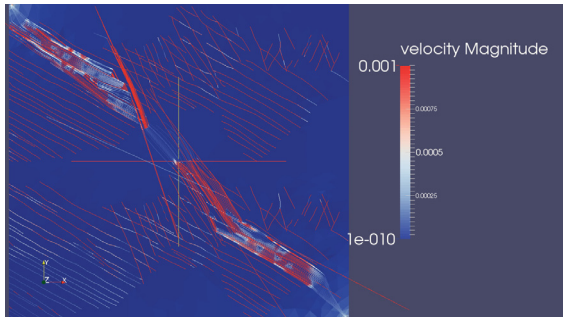
(a) Velocity magnitude ($\theta = 0°$).
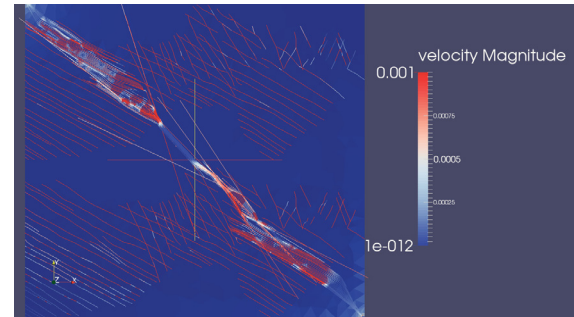
(b) Velocity magnitude ($\theta = 45°$).

Figure 4.4: Velocity magnitudes of models in fracture pattern 1 at water breakthrough.

Table 4.1: Water breakthrough time and oil production from models of fracture pattern 1.

Model	water b.t. time	oil production from model	oil production from fracture	oil production from matrix
Stress orientation $\theta = 0°$	*day*	m^3	m^3	m^3
viscous flow with capillary force (BC&WG)	164	193589	290	193299
viscous flow (BC&WG)	162	191295	309	190986
viscous flow with capillary force (PL)	140	165398	246	165152
Stress orientation $\theta = 45°$				
viscous flow with capillary force (BC&WG)	189	223143	343	222800
viscous flow (BC&WG)	188	222097	362	221735
viscous flow with capillary force (PL)	169	199641	310	199331

(a) Average oil saturation ($\theta = 0°$).
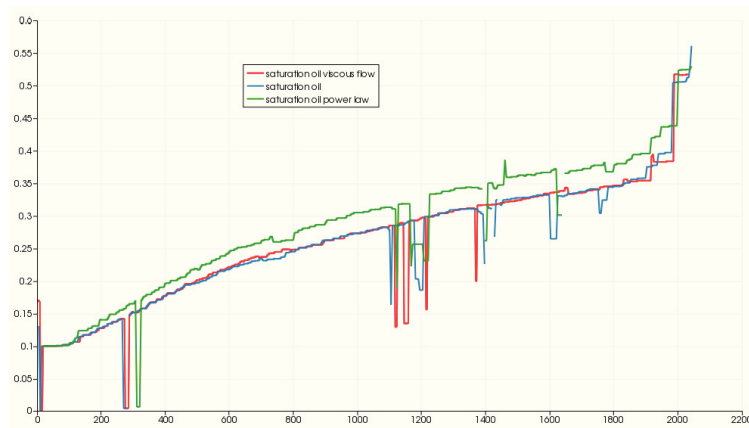
(b) Average oil saturation ($\theta = 45°$).

Figure 4.5: Average oil saturations of models under two different stress states at water breakthrough (pattern 1).
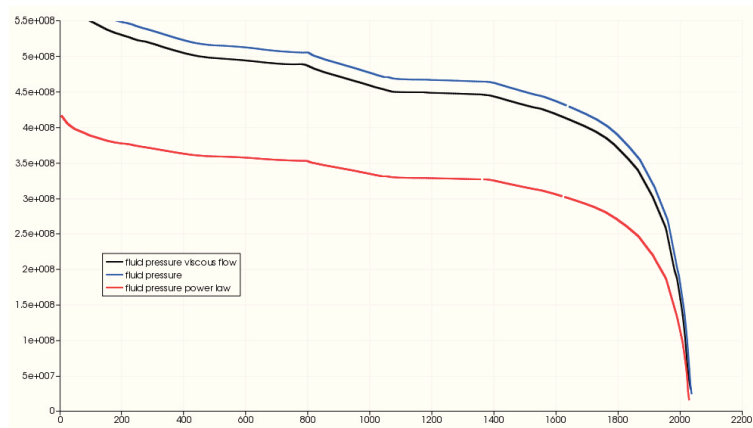
(a) Fluid pressures ($\theta = 0°$).
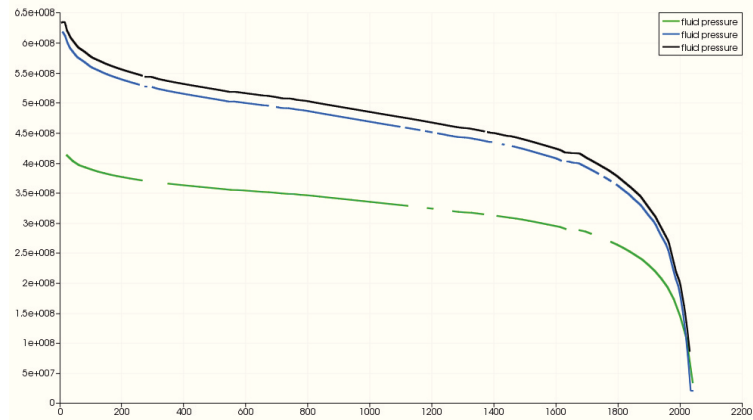
(b) Fluid pressures ($\theta = 45°$).

Figure 4.6: Fluid pressures of models under two different stress states at water breakthrough (pattern 1).

(a) Saturation profile of viscous flow using combined Brooks-Corey and Willie-Gardner relative permeability model.

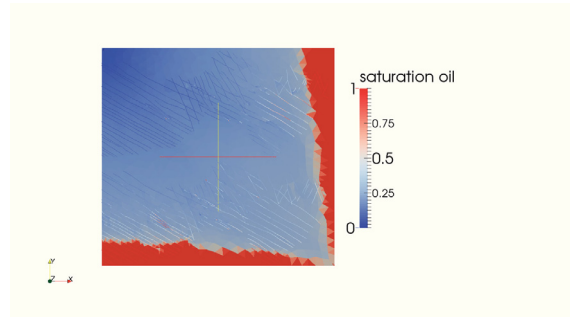(b) Saturation profile of viscous flow with capillary force (Brooks-Corey and Willie-Gardner).

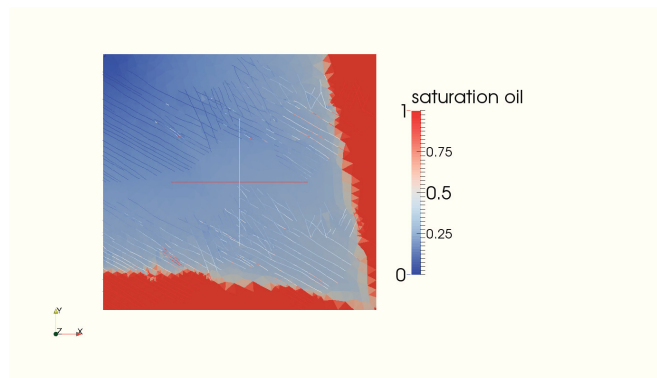(c) Saturation profile of viscous flow using power law relative permeability model.

Figure 4.7: Saturation profiles after 45 days of fluids displacement (pattern 2, $\theta = 0°$).

4.1.3 Flow Behaviors in Fracture Pattern 2 Subjected to Stress with $0°$ Orientation

In fracture pattern 2, all fractures are well interconnected, Figure 3.12 showed the permeability distribution of model under stress of $0°$ orientation. There is no extreme conductive flow channel for fluids in this flow, therefore from the saturation profile of fluids after 45 days of displacement Figure 4.7, neither the viscous flow with capillary force model using Brooks-Corey and Willie-Gardner relative permeability curve nor the model using power law relative permeability curve could be distinguished from each other. Both of these two model predicted the same amount of oil production. The only difference was that the pure viscous flow model predicted 6.75% more oil coming from fractures, despite that the total oil production from the all models were the same.

Table 4.2 lists the oil production from all the models.

From the plot of the average oil saturation and the fluid pressure along the horizontal distance from injector to producer (Figure 4.8) at water breakthrough, it can be seen that the predictions of the viscous flow models with/-out capillary force roughly coincided with each other.

50

Table 4.2: Simulation time and oil production from models (pattern 2, $\theta = 0°$).

Model	simulation time	oil production from model	oil production from fracture	oil production from matrix
Stress orientation $\theta = 0°$	day	m^3	m^3	m^3
viscous flow with capillary force (BC&WG)	45	53198	400	52798
viscous flow (BC&WG)	45	53197	427	52770
viscous flow with capillary force (PL)	45	53194	399	52795
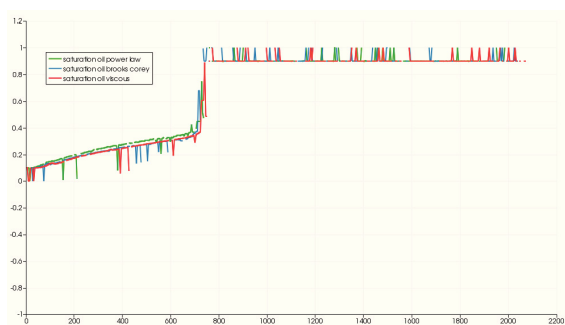
(a) Average oil saturation of viscous flow models with/-out capillary force.
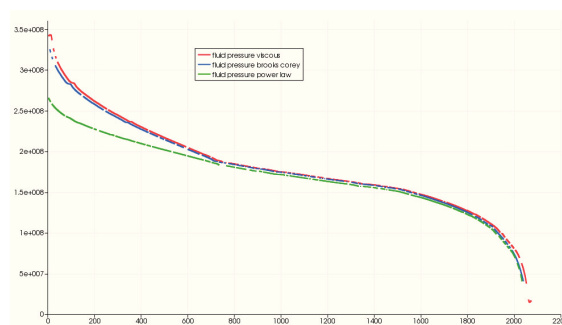
(b) Fluid pressure of viscous flow models with/-out capillary force.

Figure 4.8: Average oil saturation and fluid pressure of models after 45 days of fluids displacement. (pattern 2, $\theta = 0°$).

4.1.4 Flow Behaviors in Fracture Pattern 2 Subjected to Stress with $45°$ Orientation

In fracture pattern 2, interconnected fractures are widely distributed in model domain comparing with fracture pattern 1. The geometry is quite sensitive to the orientation of global stresses. Figure 3.13 showed the more permeable fractures are from fracture set 3 trending southward and some are from fracture set 2.

Figure 4.9 illustrate the saturation profile at water breakthrough.

Flow was highly localized along the highly conductive fractures in the models (Figure 4.10). Saturation profile showed extreme flow channeling, this was also displayed in the plot of average oil saturation and fluid pressure (Figure 4.11). Water 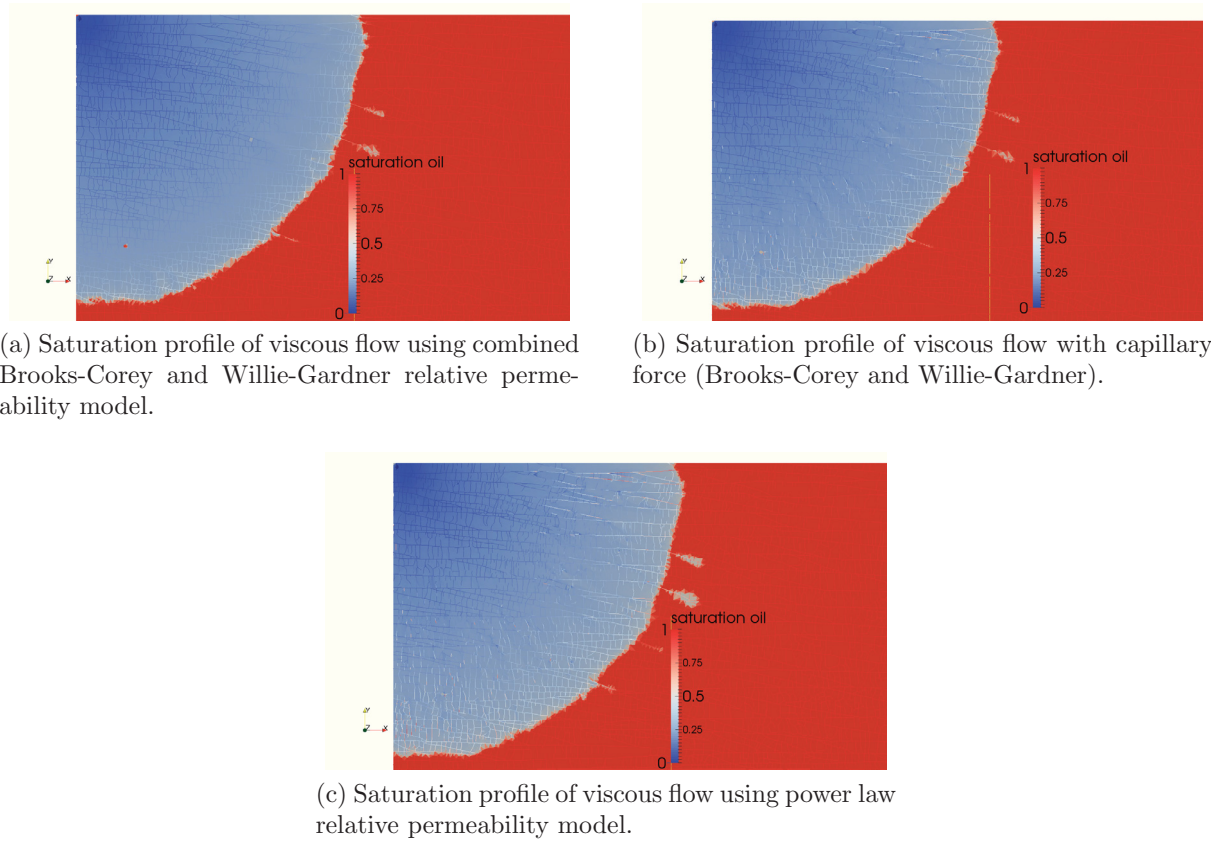breakthrough occurred much earlier than any of other models in fracture pattern 1 and models in the same fracture pattern but with 0° stress orientation. Table 4.2 summarized the water breakthrough time and the oil production from models subjected to 45° global stresses.

Table 4.3: Water breakthrough time and oil production from models (pattern 2, $\theta = 45°$).

Model	water b.t. time	oil production from model	oil production from fracture	oil production from matrix
Stress orientation $\theta = 45°$	day	m^3	m^3	m^3
viscous flow with capillary force (BC&WG)	7	8309	107	8202
viscous flow (BC&WG)	11 hours	515	372	143
viscous flow with capillary force (PL)	20	23676	174	23502

(a) Saturation profile of viscous flow (BC&WG).

(b) Saturation profile of viscous flow with capillary force (BC&WG).
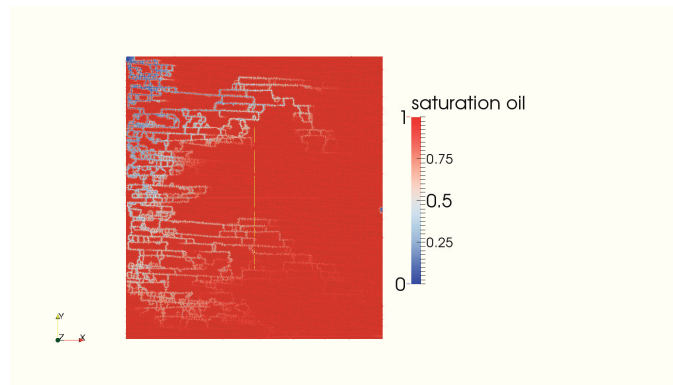
(c) Saturation profile viscous flow with capillary force (PL).

Figure 4.9: Saturation profile of models in fracture pattern 2 ($\theta = 45°$).
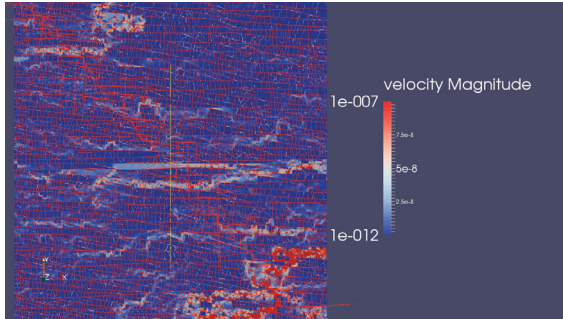
(a) Velocity magnitude of viscous flow model with capillary force (BC&WG).
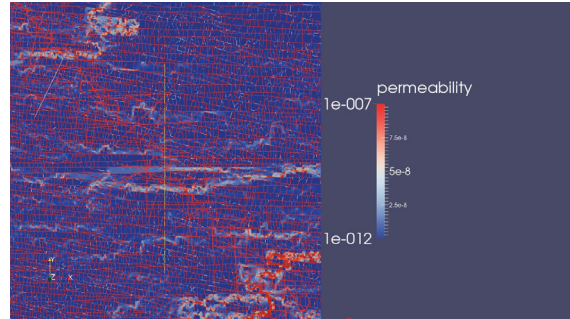
(b) Velocity magnitude viscous flow model (BC&WG).
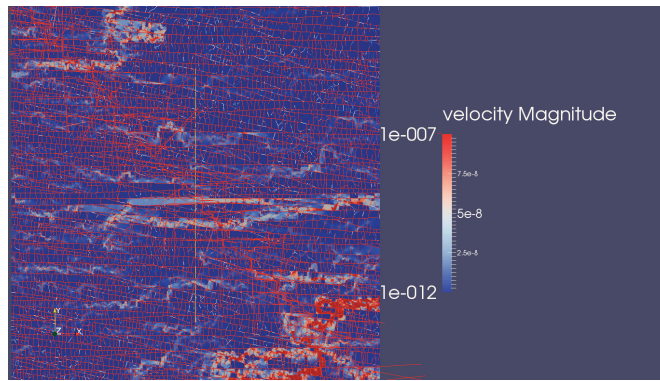
(c) Velocity magnitude viscous flow model with capillary force (PL).

Figure 4.10: Velocity magnitudes of models in fracture pattern 2 ($\theta = 45°$).
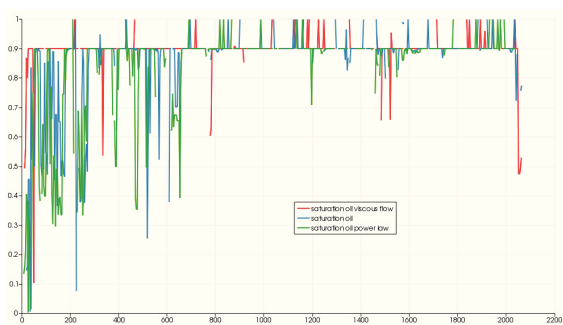
(a) Average oil saturation of models.
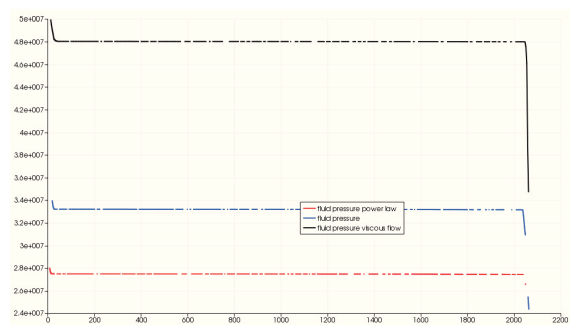
(b) Fluid pressure of models.

Figure 4.11: Average oil saturation and fluid pressure of models at water breakthrough (pattern 2, $\theta = 0°$).
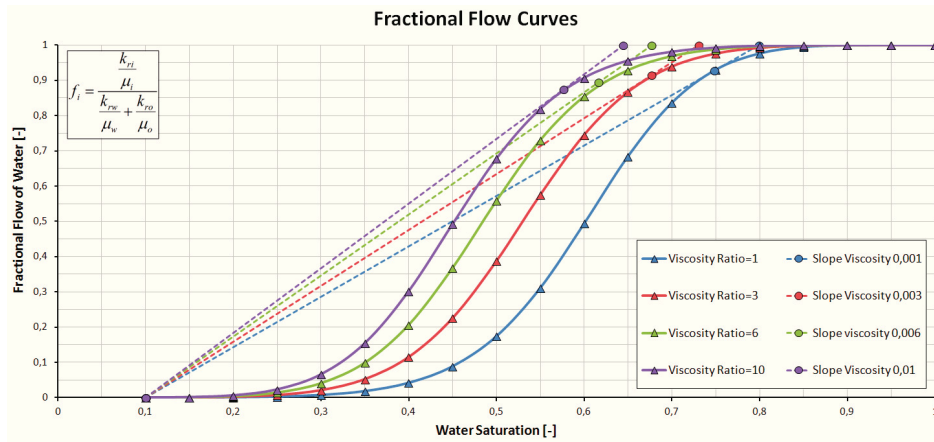
Figure 4.12: Fractional flow curves.

Because of the dominance of viscous force, much more displaced oil in viscous flow was coming from fractures. That meant injected fluid invaded more numbers of fractures in this scenario than the other two. In the previous models, power law relative permeability model predicted always earlier water breakthrough and as a consequence less oil displacement. But as the geomechanical condition changed, the permeability distribution changed as well, water breakthrough occurred on day 20 in the power law model, which was much later than both of Brooks-Corey and Willie-Gardner models.

4.2 Influence of Injection Rate and Viscosity Ratio on Areal Sweep Efficiency

From previous performed simulation results, capillary force does not play a big role in the Moab-Member sandstone in Arches area. Among all the models, in the model from fracture pattern 1, which is under 0° stress orientation, obvious viscous fingering effect was observed, it is therefore selected as candidate to run simulations to examine the influential factor for the areal sweep efficiency in this region. Injection rates and viscosity ratios are changed in the following trial simulations runs.

Previously, only one water injection rate, *i.e.*, 0.02 pore volume per year, and one viscosity ratio between oil and water, *i.e.*, 3:1, were set to all simulation runs in models.

In the following, simulations are performed by using 0.002, 0.1, 0.2 pore volume per year water injection volume respectively and meanwhile viscosity ratio is changed to 1:1, 6:1 and 10:1.

Figure 4.12 shows the fractional flow curves of different oil water viscosity ratio. The water saturation at the front and the average water saturation at the water breakthrough can be found from the tangent of each fractional flow curve. According to Equation 2.30 and Equation 2.32, areal sweep efficiency E_A can be calculated.
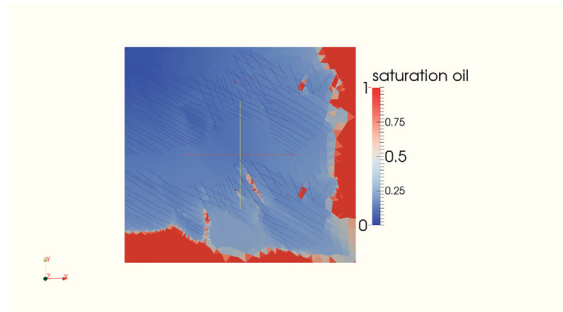
(a) Saturation profile of viscous flow with 1:1 oil water viscosity ratio.
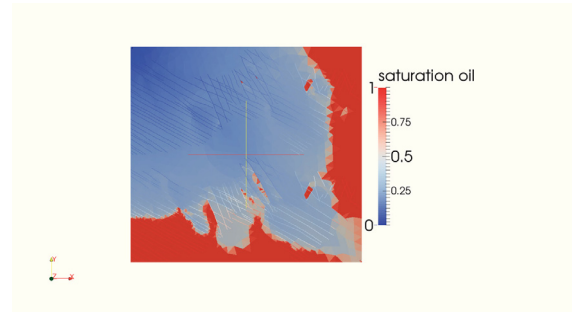
(b) Saturation profile of viscous flow with 3:1 oil water viscosity ratio.
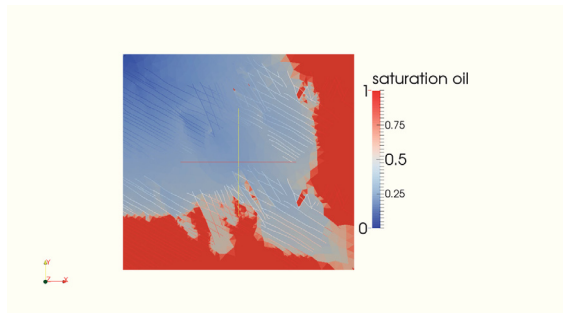
(c) Saturation profile of viscous flow with 6:1 oil water viscosity ratio.

(d) Saturation profile of viscous flow with 10:1 oil water viscosity ratio.

Figure 4.13: Saturation profiles at water breakthrough (fracture pattern 1, 0.02 PV of injected water volume).

4.2.1 Injection Water Volume of 0.02 Pore Volume

Figure 4.13 illustrates the saturation profiles of different oil water viscosity ratios at water breakthroughs. It can be observed that the higher the viscosity ratio, the severe the viscous fingering effect.

Table 4.4 lists the simulation results of each scenarios and the calculated areal sweep efficiency in each case. Both of microscopic and areal sweep efficiency decreases with the increase of viscosity ratio.

4.2.2 Injection Water Volume of 0.1 Pore Volume

Similarly, saturation profiles at water breakthrough from models with different oil water viscosity ratio are shown in Figure 4.14

Comparing Table 4.4 with Table 4.5, increasing water injection volume has increased areal sweep efficiency slightly in each scenario, except for the model with 10:1 oil-water viscosity ratio.

Table 4.4: Summary of simulation results from models with various oil water viscosity ratios (0.02 PV water injection).

0.02PV Water Injection						
viscosity ratio	water b.t. time [Day]	OOIP $[m^3]$	OIP@b.t.$[m^3]$	RE(%)	E_D	E_A (%)
1:1	Day 204	378476	137530	63.66	0.875	72.76
3:1	Day 162	378476	187181	50.54	0.7875	64.18
6:1	Day 137	378476	216662	42.75	0.7214	59.27
10:1	Day 120	378476	236717	37.46	0.6806	55.03
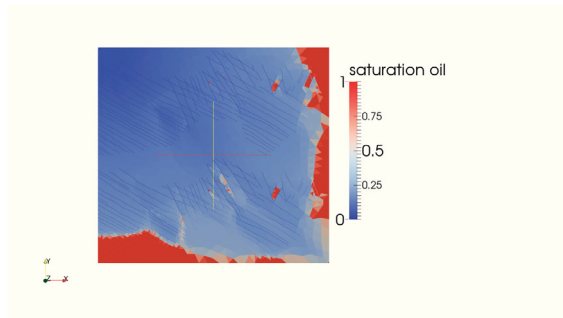
(a) Saturation profile of viscous flow with 1:1 oil water viscosity ratio.
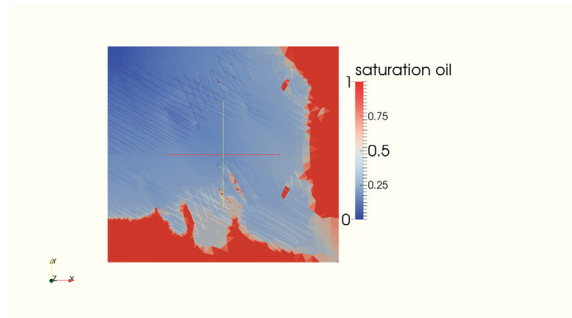
(b) Saturation profile of viscous flow with 3:1 oil water viscosity ratio.
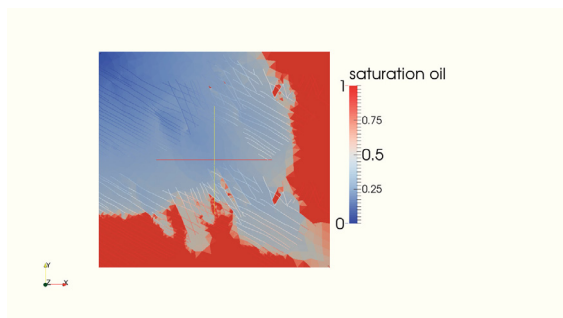
(c) Saturation profile of viscous flow with 6:1 oil water viscosity ratio.
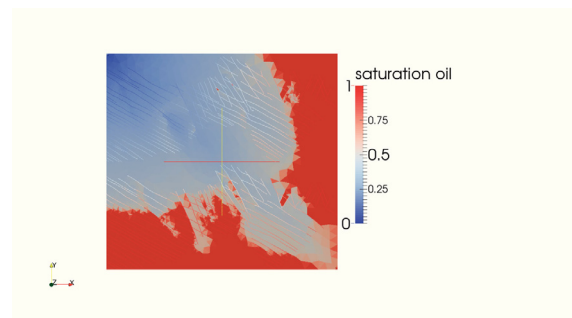
(d) Saturation profile of viscous flow with 10:1 oil water viscosity ratio.

Figure 4.14: Saturation profiles at water breakthrough (fracture pattern 1, 0.1 PV of injected water volume).

Table 4.5: Summary of simulation results from models with various oil water viscosity ratios (0.1 PV water injection).

0.1PV Water Injection						
viscosity ratio	water b.t. time [Day]	OOIP $[m^3]$	OIP@b.t.$[m^3]$	RE(%)	E_D	E_A (%)
1:1	Day 41	378476	136756	63.87	0.875	72.99
3:1	Day 33	378476	184601	51.23	0.7875	65.05
6:1	Day 28	378476	214036	43.45	0.7214	60.23
10:1	Day 24	378476	236716	37.46	0.6806	55.03

Table 4.6: Summary of simulation results from models with various oil water viscosity ratios (0.2 PV water injection).

0.2PV Water Injection						
viscosity ratio	water b.t. time [Day]	OOIP $[m^3]$	OIP@b.t.$[m^3]$	RE[%]	E_D	E_A [%]
1:1	Day 21	378476	133161	64.82	0.875	74.08
3:1	Day 17	378476	180588	52.29	0.7875	66.39
6:1	Day 14	378476	214036	43.45	0.7214	60.23
10:1	Day 12	378476	236716	37.46	0.6806	55.03

4.2.3 Injection Water Volume of 0.2 Pore Volume

Although injected water volume has been increased from 0.1 pore volume to 0.2 pore volume, at water breakthrough, not too much difference can be observed from Figure and Figure 4.15. From the simulation results (Table 4.6), increased water injection volumes didn't increase the areal sweep efficiency in scenarios with 6:1 and 10:1 oil-water viscosity ratio respectively. Areal sweep efficiencies are increased in scenarios with 1:1, which is the most favorable case for water flooding, and 3:1 oil-water viscosity ratio. However, associated with the increase of areal sweep efficiency, increasing injected water volumes leads to earlier water breakthrough time.

From performed simulations runs, for the referential model, *i.e.*, model with 0.02 pore volume injection volume and 3:1 oil-water viscosity ratio, no matter the water injection volume increased to 0.1 pore volume or to 0.2 pore volume, areal sweep efficiency was increased only 0.87% and 2.21% respectively. Figure 4.16 shows the relation between areal sweep efficiency and injected water volume for different oil-water viscosity ratios. For the higher oil-water viscosity ratios, changing injection rate has little or nearly no effect on areal sweep efficiency, like the model with 6:1 and 10:1 oil-water viscosity ratio. But, keeping the same injection rate, if the viscosity ratio decreases from 3:1 to 1:1, the areal sweep efficiency will increase roughly 8.18%.

According to the statement of Craig (1971) that areal sweep efficiency is best correlated with the average saturation mobility ration $(\overline{M})^{[2]}$. $\overline{M}$ is defined as:

$$\overline{M} = \frac{(\lambda_{rl} + \lambda_{r2})|_{S_1=\overline{S_1}}}{(\lambda_{rl} + \lambda_{r2})|_{S_1=S_{1I}}}, \tag{4.1}$$

where, λ_{rl} is the relative mobility of water, λ_{r2} is the relative mobility of oil, $\overline{S_1}$ is the average water
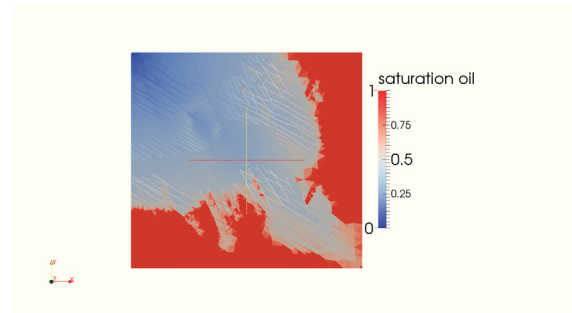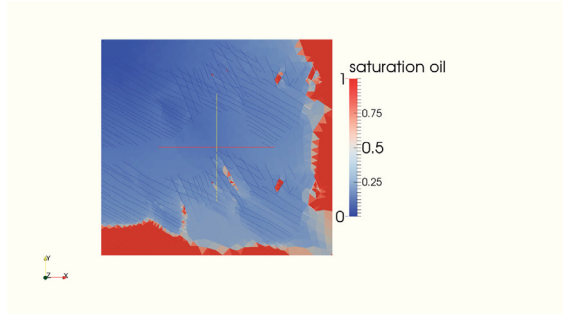
(a) Saturation profile of viscous flow with 1:1 oil water viscosity ratio.
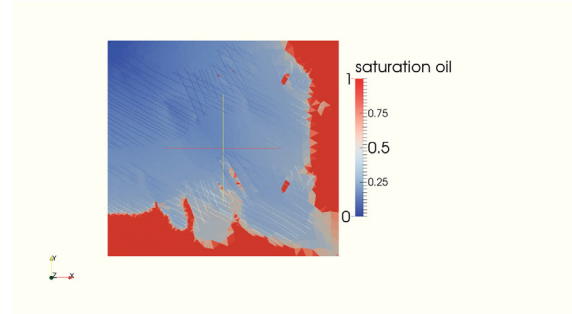
(b) Saturation profile of viscous flow with 3:1 oil water viscosity ratio.
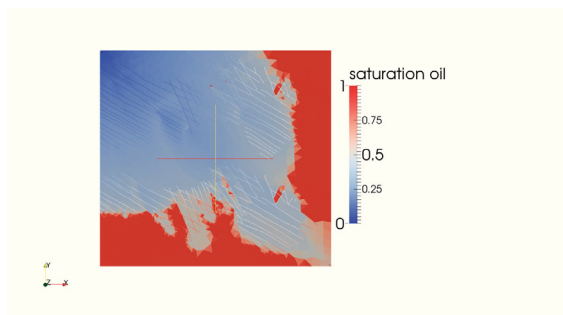
(c) Saturation profile of viscous flow with 6:1 oil water viscosity ratio.
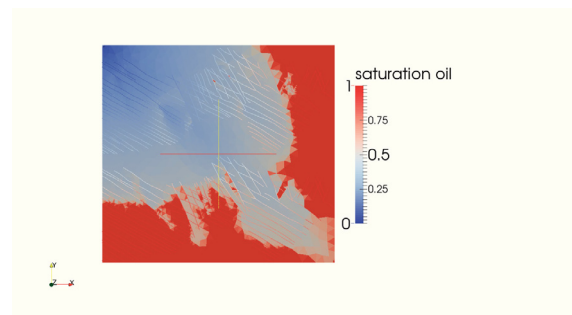
(d) Saturation profile of viscous flow with 10:1 oil water viscosity ratio.

Figure 4.15: Saturation profiles at water breakthrough (fracture pattern 1, 0.2 PV of injected water volume).
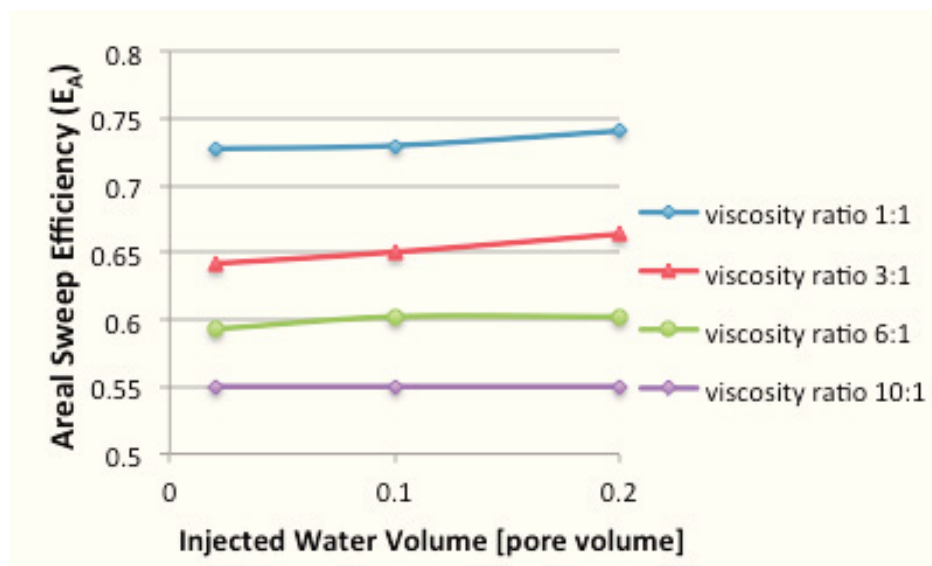
Figure 4.16: Relation between areal sweep efficiency and injected water volume.

58

Table 4.7: Convertion from viscosity ratio to average mobility ratio.

viscosity ratio	average mobility ratio $\overline{M}$
1:1	0.28
3:1	0.58
6:1	0.84
10:1	1.14

saturation and S_{1I} is the initial water saturation. The average mobility ratio is the ratio of the total relative mobility at the average water saturation behind the shock front to the total relative mobility at the initial water saturation.

Different viscosity ratios can be converted into Craig's average mobility ratios. Table 4.7 lists the corresponding values.

Figure 4.17 plots the relation between areal sweep efficiency and average mobility ratio. Generally, the change of areal sweep efficiency can not be presented appropriately by the change of average mobility ratio.
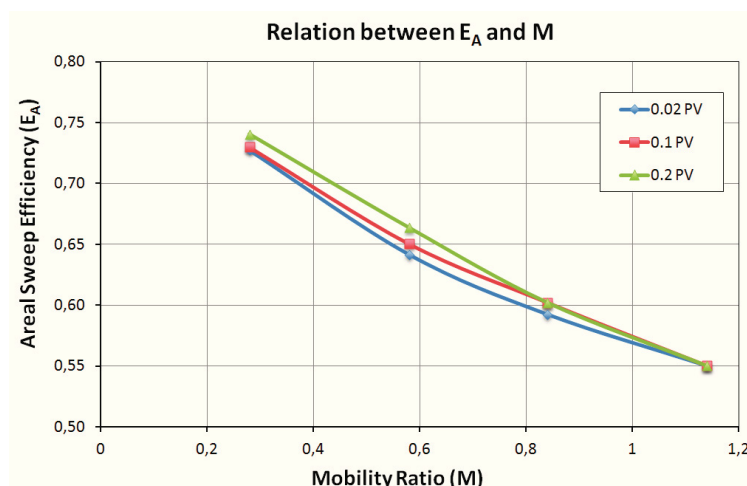

Figure 4.17: Relation between areal sweep efficiency E_A and average mobility ratio.

4.3 Comparisons of the Areal Sweep Efficiency from Simulation Results and Other Areal Sweep Efficiency Correlations

4.3.1 Willhite Correlation

By fitting the plot of calculated waterflood recoveries vs producing WOR's, which was based on experimental data from Dykstra-Parsons method, Willhite presented the correlation of areal sweep

Table 4.8: Coefficients in Fassihi's areal sweep efficiency.

Coefficient	Five-Spot
a_1	-0.2062
a_2	-0.0712
a_3	-0.511
a_4	0.3048
a_5	0.123
a_6	0.4394

efficiency at water breakthrough as[33][8]:

$$E_{Abt} = 0.54602036 + \frac{0.03170817}{M_{\overline{S}}} + \frac{0.30222997}{e^{M_S}} - 0.00509693 M_{\overline{S}} \tag{4.2}$$

where E_{Abt} is the areal sweep efficiency at breakthrough of the displacing fluid, $M_{\overline{S}}$ is the mobility ratio at the average water saturation.

4.3.2 Fassihi Correlation

By using the data of the measurements from Dyes *et al.*[12] and a use of nonlinear regression program, which matched the Dyes *et al.*, Fassihi presented a equation relating areal sweep efficiency E_A and the mobility ratio[13].

$$\frac{1 - E_A}{E_A} = [a_1 ln(M + a_2) + a3]f_w + a_4 ln(M + a_5) + a_6 \tag{4.3}$$

where M is mobility ratio and f_w is fractional flow of water at producing well.

The coefficients in the correlation differs from the flood pattern. For five-spot pattern, they are listed in Table 4.8 and for the mobility ratio between 0 and 1, these coefficients can be used for both before and after breakthrough.

4.3.3 Results Comparisons

Willhite correlation relates E_A only with mobility ratio M and Craig gave the expression of average mobility ratio $\overline{M}$ in Equation 4.1[8].

In Fassihi correlation, E_A depends not only on M but also on f_w.

Conversions of viscosity ratios to average mobility ratios $\overline{M}$ can be found in previous Table 4.7. Table 4.9 summaries the results of calculated E_A values according to Willhite correlation, Fassihi correlation and from simulation results.

The calculated results of E_A show that the water injection volumes did not play a big role in calculating E_A by using both of the two correlations. From simulation results, E_A has some different values if injected water volume changed, but only for lower oil-water viscosity ratio.

In order to examine the effect of fracture property, in this case, in terms of the fracture aperture distribution on the areal sweep efficiency, the simulations are run on the second model from the

Table 4.9: Calculation results 1 of E_A.

$\overline{M}$ Average Mobility Ratio	E_A [%] (Simulation Results)	E_A [%] (Willhite)	E_A [%] (Fassihi)
0.02 PV Water Injection			
0.28	72.76	88.63	94.21
0.58	64.18	76.7	88.67
0.84	59.27	71	85.23
1.14	55.03	66.47	82.35
0.1 PV Water Injection			
0.28	72.99	*as above*	94.27
0.58	65.05	*as above*	88.65
0.84	60.23	*as above*	85.21
1.14	55.03	*as above*	82.35
0.2 PV Water Injection			
0.28	74.08	*as above*	94.25
0.58	66.39	*as above*	88.63
0.84	60.23	*as above*	85.21
1.14	55.03	*as above*	82.35

Garden area which is under another far-field stress. As mentioned before, the water injection volume does not change the final results a lot, therefore, for the second model, only 0.02 pore volume of water is injected into model. Besides, additional simulation runs are performed with oil-water viscosity ratio 15:1 and 20:1. Calculated areal sweep efficiency E_A from both simulation results and corresponding correlations are listed in Table 4.10

The results are illustrated in Figure 4.18. From the plots of the calculated E_As, E_A values obtained from both of the correlations generally predicted much higher E_A than the ones from simulation results. Neither the Fassihi correlation nor the Willhite correlation can accurately predict the areal sweep efficiency of the models with fractures.

Comparing with the Willhite correlation, although, it over-predicted more than 11% of E_A, Fassihi correlation showed the same trend of E_A from that of the model, which is subjected to 45° stress and has less heterogeneous aperture distribution. On the other hand, Willhite correlation

Table 4.10: Calculation results 2 of E_A.

$\overline{M}$ Average Mobility Ratio	E_A [%] Simulation Results (Stress 0)	E_A [%] Simulation Results (Stress 45)	E_A [%] Willhite	E_A [%] Fassihi (Stress 0/45)
0.02 PV Water Injection				
0.28	72.76	81.58	88.63	94.21/94.19
0.58	64.18	74.52	76.7	88.67/88.49
0.84	59.27	71.30	71	85.23/84.94
1.14	55.03	68.23	66.47	82.35/81.95
1.37	52.74	66.86	63.90	80.70/80.22
1.65	52.58	67.83	61.49	79.01/78.45
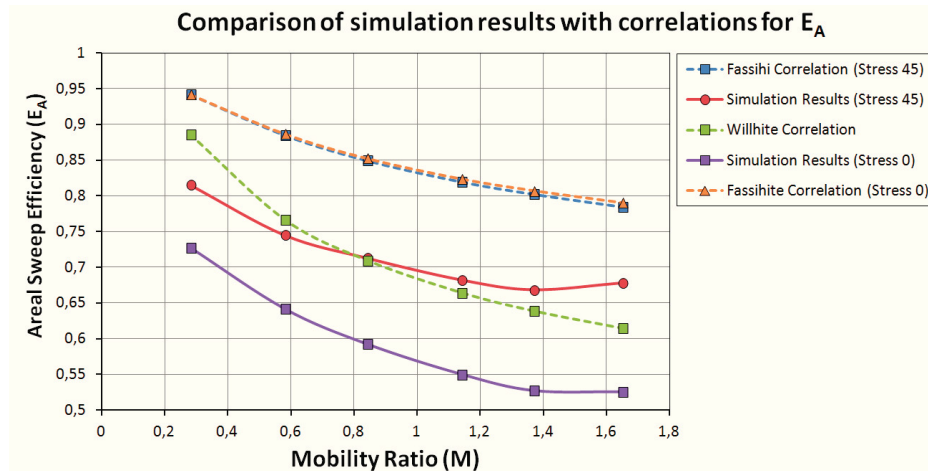
Figure 4.18: Comparison of simulation results with correlations for E_A.

has the same trend line of E_A as that from the model which is subjected to 0° stress and has more heterogeneous aperture distribution.

4.4 Quantification of Effect of Fracture Aperture on Areal Sweep Efficiency

4.4.1 Examination of the Sensitivity of Simulation Results to the Change of Fracture Aperture

The main difference between the Fassihi correlation and simulation results, which showed in Figure 4.18, is that the Fassihi correlation does not include fracture properties. In order to quantify the effect of the change of fracture aperture on the areal sweep efficiency, a 2D test model (Figure 4.19) is created with dimension of 10*10 meters and only 1 fracture is assumed inside this model.

For the simulation runs with the test model, all other parameters are set to the same like the previous simulations based on the models from the Garden area in Arches National Park. As to the fracture aperture, instead of by using fracture aperture distribution, fracture aperture is assumed to be constant for each simulation run.

Table 4.11 listed the calculated results of E_A from the test model, if fracture aperture is set to be 1 mm, 3 mm, 5 mm, 8 mm and 10 mm. In this case, only viscous flow is considered.

The relations between E_As calculated either from Fassihi correlation or from simulation results and oil-water mobility ratio are plotted in Figure 4.20. It showed that areal sweep efficiency E_A shifted more or less parallel downward from the Fassihi correlation. E_A is in direct proportion to the size of fracture aperture. The bigger the fracture aperture, the larger the E_A will be. Meanwhile, E_A is inversely proportional to the oil-water mobility ratio.
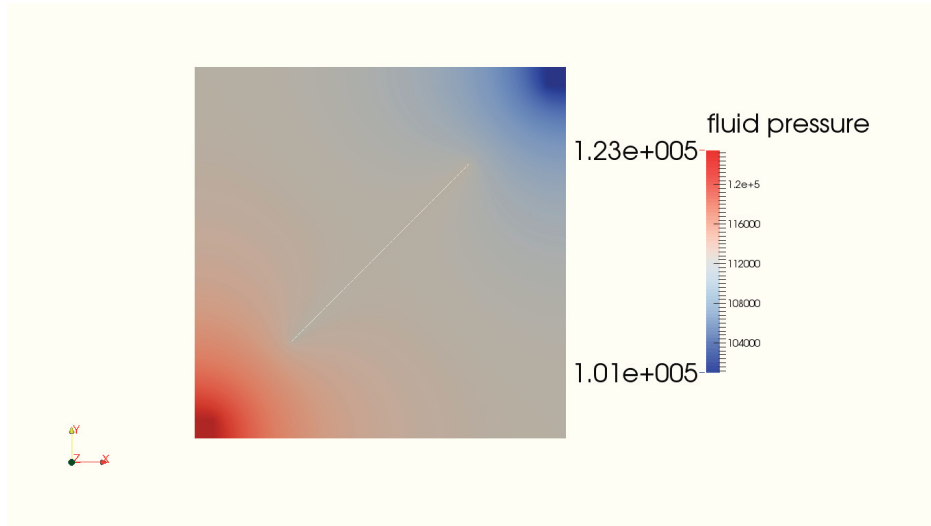
Figure 4.19: 10m*10m test model with only 1 fracture inside.
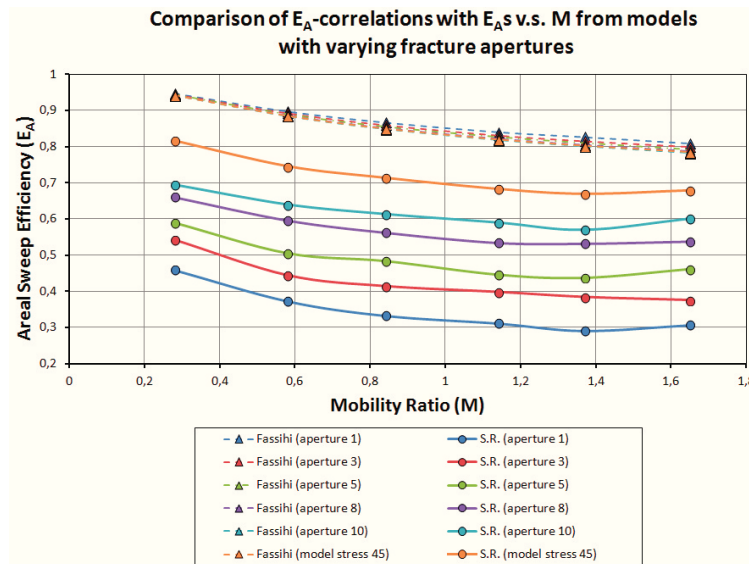
Figure 4.20: Comparison of Fassihi correlation with E_As from test model with varying fracture apertures.

Table 4.11: Calculation results of E_A in test model.

$\overline{M}$ Average Mobility Ratio	E_A [%] Fassihi	E_A [%] Simulation Results	E_A(Fassihi)-E_A(Simulation)[%]
Fracture Aperture =1 mm			
0.28	94.69	45.89	48.80
0.58	89.73	37.30	52.43
0.84	86.68	33.28	53.40
1.14	84.02	31.15	52.87
1.37	82.65	29.10	53.54
1.65	80.90	30.70	50.20
Fracture Aperture =3 mm			
0.28	94.48	54.23	40.25
0.58	89.25	44.44	44.81
0.84	85.96	41.42	44.54
1.14	83.12	39.81	43.30
1.37	81.53	38.43	43.11
1.65	79.97	37.55	42.42
Fracture Aperture =5 mm			
0.28	94.37	58.93	35.44
0.58	88.93	50.59	38.35
0.84	85.50	48.44	37.06
1.14	82.68	44.70	37.98
1.37	81.01	43.83	37.18
1.65	79.20	46.24	32.96
Fracture Aperture =8mm			
0.28	94.24	66.02	28.21
0.58	88.58	59.59	29.00
0.84	85.09	56.23	28.86
1.14	82.13	53.40	28.74
1.37	80.38	53.18	27.21
1.65	78.64	53.77	24.86
Fracture Aperture =10 mm			
0.28	94.18	69.40	24.77
0.58	88.44	64.00	24.43
0.84	84.87	61.39	23.49
1.14	81.87	59.05	22.82
1.37	80.15	57.04	23.10
1.65	78.3	60.12	18.18
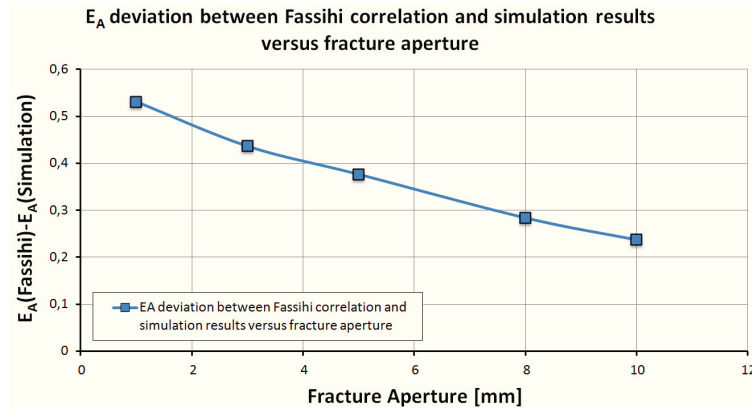
Figure 4.21: Plot of average E_A deviation from Fassihi correlation and fracture apertures.
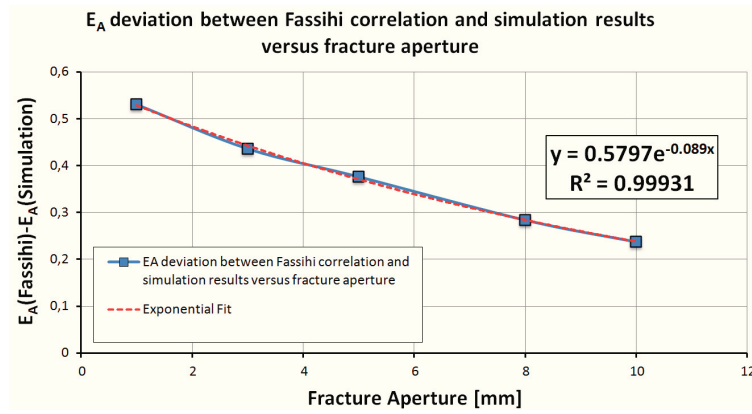
Figure 4.22: Plot of E_A deviation from Fassihi correlation as function of fracture aperture.

4.4.2 Modification of Fassihi Correlation for the Models with Fractures

Figure 4.21 plots the relation between the average deviation of E_A in individual fracture aperture and the fracture apertures.

Figure 4.22 showed that the average deviation of E_A in individual fracture aperture can be expressed as an exponential function of fracture aperture:

$$E_A(Fassihi) - E_A(Simulation) = f(a), \tag{4.4}$$

where "a" refers to the value of fracture aperture.

Equation 4.4 can also be written as:

$$E_A(Simulation) = E_A(Fassihi) - f(a) \tag{4.5}$$

According to Equation 4.3, $E_A(Fassihi)$ is defined as:

$$E_A(Fassihi) = \frac{1}{1 + [a_1 ln(M + a_2) + a_3]f_w + a_4 ln(M + a_5) + a_6}, \tag{4.6}$$

Table 4.12: Verification of modified Fassihi correlation to predict E_A.

$\overline{M}$ Average Mobility Ratio	E_A [%] Fassihi	E_A [%] Simulation Results	E_A [%] Prediction	Error [%]
Fracture Aperture =15 mm				
0.58	88.19	72.23	72.97	0.97
Fracture Aperture =20 mm				
0.58	88.03	78.52	78.25	0.34

where the coefficients a_1, a_2, a_3, a_4, a_5, a_6 are found in Table 4.8.

Fassihi correlation was originally based on conventional reservoir models without consideration of fractures in models, like the results showed that it will over-predict the areal sweep efficiency E_A for the models with fractures inside.

Based on all the simulation results which are performed in this thesis, f(a) is obtained by:

$$f(a) = 0.5797e^{-0.089a} \tag{4.7}$$

Therefore, from Equation 4.6 and Equation 4.7, Fassihi correlation can be modified to predict areal sweep efficiency E_A for the models with fractures:

$$E_A = \frac{1}{1 + [a_1 ln(M + a_2) + a_3]f_w + a_4 ln(M + a_5) + a_6} - 0.5797e^{-0.089a} \tag{4.8}$$

In order to verify the applicability of Equation 4.8, extra simulations are carried out by using 15 mm and 20 mm fracture apertures respectively. Previous simulation results showed that the average oil-water mobility ratio does not affect the difference between the E_A based on Fassihi correlation and the E_A obtained from simulations much. For the extra simulations, only one average oil-water mobility ratio was used. Results are listed in Table 4.12.

In the Equation 4.7, as a parameter, "a" can be either a constant value, e.g., like the one which is used in the simple test model or a more complex expression of fracture aperture distribution, e.g., the one which is used for the models in Garden area in Arches National Park.

Chapter 5

Discussion

The purpose of this thesis was to examine the influence of fracture patterns' geometries on the flow behaviors in naturally fractured reservoir and the models sensitivity to different relative permeability curves. Consequently, simulations were not focused on accuracy of oil recoveries of different scenarios, but they were conducted based on some simplifications. Secondly, models were in 2D and in the 3D reality, parameters are more heterogeneous. For instance, fingering in the plane of fractures can not expressed in 2D models.

In this thesis, relative permeability model for fractures was treated as linear, which ignores the effect of roughness of the fracture surfaces and zero capillary pressure. Like Porte *et al*[10] pointed out that this may lead to prediction error of oil recovery.

Fluid properties used in all simulations were moderate. The viscosity ratio between oil and water was 3:1, although studies demonstrated that viscosity ratio between oil and water has effect on saturation front in the process of water-drive. Belayneh, Geiger and Matthäi[5] compared the effect of viscosity ratio on shape of saturation front and concluded: if there is contrast between the two fluids, small differences in the velocity of the saturation front get amplified, and viscous fingers develop. They suggested the best condition for water flooding in fractures when the viscosity ratio is 1. Higher oil viscosity relative to that of water will increase the contrast of total mobility of fracture and matrix. Oil therefore trends to be trapped in rock matrix.

Simulation results from fracture pattern 1 (Figure 4.1) showed the presence of viscous fingering, with the decreasing of viscosity ratio between oil and water from 3:1 to 1:1, the saturation front at water breakthrough in this case should tend to be more stable.

Different permeability distributions of the two geometries in fracture pattern 2 resulted in quite different saturation fronts. From comparison of plot 3.8 and 3.9, fractures in the model subjected to 45° stress are generally more permeable than that of in model subjected to 0° stress. This led to faster water breakthrough and lower recovery. On the other hand, in the latter model, simulation results showed roughly the same amount of oil production from both the viscous flow model and the viscous flow model with capillary force (Table 4.2, 4.3). This indicates that the effect of fracture and matrix transfer is not pronounced if fractures have higher conductivity. The studies carried by Matthäi, Bazrafkan and Lang (2012) in the same region, also proved that in the km-scale model in Moab sandstone, viscous force is more significant than the capillary fracture matrix transfer[20]. This explained the invade of injected water into high number of fractures in the aforementioned model, which encountered much earlier water breakthrough.

Chapter 6

Conclusion

Simulations of oil displacement by water in 2D discrete models of naturally fractured reservoir analog with/-out well developed fracture networks indicate the influence of the presence of fracture networks on the production behavior. In these mainly field-data based simulations, conclusions can be drawn as following:

1. Fracture aperture distribution changes with the changing of its position relative to the global stresses. Even in the same fracture network pattern, if the imposed global far-field stress change its orientation, fracture aperture distribution will be different. In simulations, this will result in different permeability distributions.

2. From the response of the two chosen fracture patterns to the changes of stress states, fracture permeability distribution is more easily affected by the changing stress state from the well intersected fractures network.

3. Generally, capillary force doesn't play a big role in fluid displacement process in the fracture patterns from the outcrop of Salt Vally anticline in Arches National Park. Simulation models with/-out capillary force predicted little different referring to oil displacement.

4. Viscous flow is more dominant comparing with capillary fracture matrix transfer in these DFM models, especially in the models with well intersected fractures and higher fracture conductivity.

5. Power-law relative permeability model predicted normally earlier water breakthrough in all the simulation models, except when viscous force becomes absolutely dominant, power-law model would predict later water breakthrough time than Brooks-Corey and Willie-Gardner model.

6. Increasing injected fluids volume has limited effect in terms of areal sweep efficiency in models having permeable flowing paths if oil-water viscosity is high.

7. Under certain assumptions, Fassihi correlation can be modified by including factor, like fracture aperture to predict the E_A for simulation models described in this thesis when the average mobility ratio $\overline{M}$ lies in the range of 0 and 1.5.

Nomenclature

α interporosity flow factor $[m^{-1}]$

Δ_h hydraulic head difference [mm]

γ surface tension [N/m]

λ_t total mobility [X]

λ_{r1} relative mobility of water [X]

λ_{r2} relative mobility of oil [X]

μ dynamic fluid viscosity $[Pasec^{-1}]$

ω storativity ratio [X]

$\overline{k}_m$ average matrix permeability [X]

$\overline{M}$ average mobility ratio [X]

$\overline{S}_w$ average water saturation [X]

ϕ porosity [X]

ρ density $[kgm^{-3}]$

σ shape factor $[mm^{-2}]$

τ_o gravity drainage rate [STB/D]

a fracture aperture [mm]

b_0 mean half fracture aperture [mm]

C proportional constant in cubic law [X]

c compressibility $[Pa^{-1}]$

c_t total system compressibility $[Pa^{-1}]$

E_{Abt} areal sweep efficiency at water breakthrough [X]

f_i fractional flow function [X]

g	acceleration of gravity $[ms^{-2}]$
H	fracture height [mm]
k_r	relative permeability $[m^2]$
l	fracture length [m]
$M_{\overline{S}}$	mobility ratio at average water saturation [X]
P_c	capillary pressure [Pa]
P_{cfD}	dimensionless fracture capillary pressure [X]
Q	flow rate [m/s]
q	fluid source/sink $[m^{-3}sec^{-1}]$
R_1	average pore radius [mm]
r_1	radius of curved interface curvature at point 1 [mm]
R_2	average pore-throat radius [mm]
r_2	radius of curved interface curvature at point 2 [mm]
S_1	average water saturation [X]
S_w	water saturation [X]
S_{1I}	initial water saturation [X]
S_{or}	irreducible oil saturation [X]
S_{wirr}	irreducible water saturation [X]
T	fracture transmissivity [X]
t	time [s]
u	darcy flux vector $[m^3sec^{-1}]$
v	darcy velocity $[ms^{-1}]$
w	fracture width [mm]
W_{ibt}	injected water volume at breakthrough $[m^3]$
W_{inj}	injected water volume $[m^3]$

Bibliography

[1] Tarek Ahmed et al. *Reservoir engineering handbook*. Gulf Professional Publishing, 2006.

[2] Emad W Al-Shalabi, Kamy Sepehrnoori, Gary Pope, et al. An improved method for estimating volumetric sweep efficiency of low salinity water injection (russian). In *SPE Annual Caspian Technical Conference and Exhibition*. Society of Petroleum Engineers, 2014.

[3] Marco Antonellini and Atilla Aydin. Effect of faulting on fluid flow in porous sandstones: petrophysical properties. *AAPG bulletin*, 78(3):355–377, 1994.

[4] GI Barenblatt, Iu P Zheltov, and IN Kochina. Basic concepts in the theory of seepage of homogeneous liquids in fissured rocks [strata]. *Journal of applied mathematics and mechanics*, 24(5):1286–1303, 1960.

[5] Mandefro Belayneh, Sebastian Geiger, and Stephan K Matthäi. Numerical simulation of water injection into layered fractured carbonate reservoir analogs. *AAPG bulletin*, 90(10):1473–1493, 2006.

[6] Mandefro W Belayneh, Stephan K Matthai, Martin J Blunt, and Stephen F Rogers. Comparison of deterministic with stochastic fracture models in water-flooding numerical simulations. *AAPG bulletin*, 93(11):1633–1648, 2009.

[7] Bernard J Bourbiaux, Francois J Kalaydjian, et al. Experimental study of cocurrent and countercurrent flows in natural porous media. *SPE Reservoir Engineering*, 5(03):361–368, 1990.

[8] Forrest Craig. The reservoir engineering aspects of waterflooding spe monograph series, volume 3. *Society of Petroleum*, 1971.

[9] Kenneth M Cruikshank, Guozhu Zhao, and Arvid M Johnson. Analysis of minor fractures associated with joints and faulted joints. *Journal of Structural Geology*, 13(8):865–886, 1991.

[10] Jacoba de la Porte, Charles Kossack, and Robert Zimmerman. The effect of fracture relative permeabilities and capillary pressures on the numerical simulation of naturally fractured reservoirs. In *SPE Annual Technical Conference and Exhibition*, 2005.

[11] RH Dean, LL Lo, et al. Simulations of naturally fractured reservoirs. *SPE reservoir engineering*, 3(02):638–648, 1988.

[12] AB Dyes, BH Caudle, RA Erickson, et al. Oil production after breakthrough as influenced by mobility ratio. *Journal of Petroleum Technology*, 6(04):27–32, 1954.

[13] MR Fassihi et al. New correlations for calculation of vertical coverage and areal sweep efficiency. *SPE reservoir engineering*, 1(6):604–606, 1986.

[14] James R Gilman. Practical aspects of simulation of fractured reservoirs. In *International Forum on Reservoir Simulation, Buhl, Baden-Baden, Germany*, pages 23–27, 2003.

[15] James Russell Gilman, Huabing Wang, Sepehr Fadaei, Michael James Uland, et al. A new classification plot for naturally fractured reservoirs. In *Canadian Unconventional Resources Conference*. Society of Petroleum Engineers, 2011.

[16] M Karimi-Fard and Abbas Firoozabadi. Numerical simulation of water injection in 2d fractured media using discrete-fracture model. In *SPE annual technical conference and exhibition*, 2001.

[17] Christian Klimczak, Richard A Schultz, Rishi Parashar, and Donald M Reeves. Cubic law with aperture-length correlation: implications for network scale fluid flow. *Hydrogeology Journal*, 18(4):851–862, 2010.

[18] John C Lorenz and Scott P Cooper. Interpreting fracture patterns in sandstones interbedded with ductile strata at the salt valley anticline, arches national park, utah. 2001.

[19] Charles Marle. *Multiphase flow in porous media*. Éditions technip, 1981.

[20] SK Matthai, S Bazrafkan, P Lang, and C Milliotte. Numerical prediction of relative permeability in water-wet naturally fractured reservoir rocks. In *ECMOR XIII-13th European Conference on the Mathematics of Oil Recovery*, 2012.

[21] Stephan K Matthai. Multiphase flow behaviour of naturally fractured reservoir. In *Three-Day Technology Seminar,February 21-23rd 2011, seminar handouts ,Kuala Lumpur, Malaysia*, 2011.

[22] David B McWhorter and Daniel K Sunada. Exact integral solutions for two-phase flow. *Water Resources Research*, 26(3):399–413, 1990.

[23] Ronald Nelson. *Geologic analysis of naturally fractured reservoirs*. Gulf Professional Publishing, 2001.

[24] PM Oen, M Engell-Jensen, AA Barendregt, et al. Skjold field danish north sea: Early evaluations of oil recovery through water imbibition in a fractured reservoir. *SPE Reservoir Engineering*, 3(01):17–22, 1988.

[25] A Paluszny, SK Matthäi, and M Hohmeyer. Hybrid finite element–finite volume discretization of complex geologic structures and a new simulation workflow demonstrated on fractured rocks. *Geofluids*, 7(2):186–208, 2007.

[26] Sonja Leonie Philipp, Filiz Afsar, and Agust Gudmundsson. Effects of mechanical layering on hydrofracture emplacement and fluid transport in reservoirs. *Frontiers in Earth Science*, 1, 2013.

[27] David D Pollard and Atilla Aydin. Progress in understanding jointing over the past century. *Geological Society of America Bulletin*, 100(8):1181–1204, 1988.

[28] M Pooladi-Darvish, A Firoozabadi, et al. Experiments and modelling of water injection in water-wet fractured porous media. *Journal of Canadian Petroleum Technology*, 39(3):31–42, 2000.

[29] Pallav Sarma. *New transfer functions for simulation of naturally fractured reservoirs with dual porosity models.* PhD thesis, STANFORD UNIVERSITY, 2003.

[30] Brij Bhusan Saran Singhal and Ravi P Gupta. *Applied hydrogeology of fractured rocks*, volume 430. Springer, 2010.

[31] Anton van Heel, Paulus Boerrigter, and Paulus Boerrigter. On the shape-factor in fractured reservoir simulation. In *SPE Annual Technical Conference and Exhibition*, 2006.

[32] Antoon P van Heel, Paulus M Boerrigter, Johan J van Dorp, et al. Thermal and hydraulic matrix-fracture interaction in dual-permeability simulation. *SPE Reservoir Evaluation & Engineering*, 11(04):735–749, 2008.

[33] GP Willhite. Waterflooding, volume 3 of spe textbook series. *Society of Petroleum Engineers, Richardson, TX*, 1986.

[34] PA Witherspoon. Validity of cubic law for fluid flow in a deformable rock fracture. *Lawrence Berkeley National Laboratory*, 2010.

[35] Guozhu Zhao and Arvid M Johnson. Sequence of deformations recorded in joints and faults, arches national park, utah. *Journal of Structural Geology*, 14(2):225–236, 1992.

[36] Robert W Zimmerman. The history and role of the cubic law for fluid flow in fractured rocks. 2012.

[37] Robert W Zimmerman and Gudmundur S Bodvarsson. Hydraulic conductivity of rock fractures. *Transport in porous media*, 23(1):1–30, 1996.

Appendix A

```
 1  #————————————————————————————————————————————————
 2  # (1) global material properties
 3  #————————————————————————————————————————————————
 4  porosity                                          1.
 5  brooks corey parameter                            0.
 6  entry pressure                                    0.
 7  residual saturation non−wetting phase             0.
 8  residual saturation wetting phase                 0.
 9  volume modifier                                   0.01
10  saturation oil                                    1.
11  saturation water                                  0.
12  rock type                                         2.
13  density water                                     1000.
14  density oil                                       850.
15  viscosity water                                   1.0e−3
16  viscosity oil                                     3.0e−3
17  fluid pressure                                    0.
18  nodal fluid volume source                         0.
19  fluid volume source                               0.
20  oil volume source                                 0.
21  water volume source                               0.
22  saturation                                        0.
23
24  #————————————————————————————————————————————————
25  # (2) local material properties (of the fractures and matrix)
26  #————————————————————————————————————————————————
27  MATRIX complete permeability                       7.e−13
28  MATRIX complete porosity                           0.2
29  MATRIX complete saturation water                   0.1
30  MATRIX complete saturation oil                     0.9
31  MATRIX complete residual saturation wetting phase      0.1
32  MATRIX complete residual saturation non−wetting phase  0.1
33  MATRIX complete brooks corey parameter             2.0
34  MATRIX complete boundary source                    0.
35  MATRIX complete entry pressure                     2000.
36  MATRIX complete volume modifier                    1.
37  MATRIX complete rock type                          0.
38  INJ    complete permeability                       8.33e−4
39  INJ    complete porosity                           1.
40  INJ    complete brooks corey parameter             0.
41  INJ    complete entry pressure                     0.
42  INJ    complete residual saturation non−wetting phase  0.
43  INJ    complete residual saturation wetting phase      0.
44  INJ    complete saturation oil                     0.
45  INJ    complete saturation water                   1.
46  INJ    complete water volume source                5.47e−4
47  INJ    complete volume modifier                    1.
48  PROD   complete permeability                       8.33.e−4
49  PROD   complete porosity                           1.
```

```
50  PROD    complete entry pressure                         0.
51  PROD    complete residual saturation non−wetting phase  0.
52  PROD    complete residual saturation wetting phase      0.
53  PROD    complete saturation oil                         1.
54  PROD    complete saturation water                       0.
55  PROD    complete volume modifier                        1
56  PROD    complete fluid pressure                         1.5e7
57
58  #————————————————————————————————————————————————————
59  # (4) essential conditions on model boundaries
60  #————————————————————————————————————————————————————
61
62  #————————————————————————————————————————————————————
63  # (5) essential flags
64  #————————————————————————————————————————————————————
65  PROD    complete fluid pressure        Dirichlet
66
67  #————————————————————————————————————————————————————
68  # (6) computational settings
69  #————————————————————————————————————————————————————
70  time stepping conservative
71  duration 51148800
72  output time 600
73  output time 1200
74  output time 1800
75  output time 2400
76  output time 3000
77  output time 3600
78  output time 4200
79  output time 4800
80  output time 5400
81  output time 6000
82  output time 12000
83  output time 18000
84  output time 24000
85  output time 30000
86  output time 36000
87  output time 42000
88  output time 48000
89  output time 54000
90  output time 60000
91  output time 66000
92  output time 72000
93  output time 78000
94  output time 84000
95  output time 86400
96  output time 172800
97  output time 259200
98  output time 345600
99  output time 432000
100 output time 518400
101 output time 604800
102 output time 691200
103 output time 777600
104 output time 864000
105 output time 950400
106 output time 1036800
107 output time 1123200
108 output time 1209600
109 output time 1296000
110 output time 1382400
111 output time 1468800
112 output time 1555200
113 output time 1641600
114 output time 1728000
```

```
115   output  time  1814400
116   output  time  1900800
117   output  time  1987200
118   output  time  2073600
119   output  time  2160000
120   output  time  2246400
121   output  time  2332800
122   output  time  2419200
123   output  time  2505600
124   output  time  2592000
125   output  time  2678400
126   output  time  2764800
127   output  time  2851200
128   output  time  2937600
129   output  time  3024000
130   output  time  3110400
131   output  time  3196800
132   output  time  3283200
133   output  time  3369600
134   output  time  3456000
135   output  time  3542400
136   output  time  3628800
137   output  time  3715200
138   output  time  3801600
139   output  time  3888000
140   output  time  3974400
141   output  time  4060800
142   output  time  4147200
143   output  time  4233600
144   output  time  4320000
145   output  time  4406400
146   output  time  4492800
147   output  time  4579200
148   output  time  4665600
149   output  time  4752000
150   output  time  4838400
151   output  time  4924800
152   output  time  5011200
153   output  time  5097600
154   output  time  5184000
155   output  time  5270400
156   output  time  5356800
157   output  time  5443200
158   output  time  5529600
159   output  time  5616000
160   output  time  5702400
161   output  time  5788800
162   output  time  5875200
163   output  time  5961600
164   output  time  6048000
165   output  time  6134400
166   output  time  6220800
167   output  time  6307200
168   output  time  6393600
169   output  time  6480000
170   output  time  6566400
171   output  time  6652800
172   output  time  6739200
173   output  time  6825600
174   output  time  6912000
175   output  time  6998400
176   output  time  7084800
177   output  time  7171200
178   output  time  7257600
179   output  time  7344000
```

```
180 | output time 7430400
181 | output time 7516800
182 | output time 7603200
183 | output time 7689600
184 | output time 7776000
185 | output time 7862400
186 | output time 7948800
187 | output time 8035200
188 | output time 8121600
189 | output time 8208000
190 | output time 8294400
191 | output time 8380800
192 | output time 8467200
193 | output time 8553600
194 | output time 8640000
195 | output time 8726400
196 | output time 8812800
197 | output time 8899200
198 | output time 8985600
199 | output time 9072000
200 | output time 9158400
201 | output time 9244800
202 | output time 9331200
203 | output time 9417600
204 | output time 9504000
205 | output time 9590400
206 | output time 9676800
207 | output time 9763200
208 | output time 9849600
209 | output time 9936000
210 | output time 10022400
211 | output time 10108800
212 | output time 10195200
213 | output time 10281600
214 | output time 10368000
215 | output time 10454400
216 | output time 10540800
217 | output time 10627200
218 | output time 10713600
219 | output time 10800000
220 | output time 10886400
221 | output time 10972800
222 | output time 11059200
223 | output time 11145600
224 | output time 11232000
225 | output time 11318400
226 | output time 11404800
227 | output time 11491200
228 | output time 11577600
229 | output time 11664000
230 | output time 11750400
231 | output time 11836800
232 | output time 11923200
233 | output time 12009600
234 | output time 12096000
235 | output time 12182400
236 | output time 12268800
237 | output time 12355200
238 | output time 12441600
239 | output time 12528000
240 | output time 12614400
241 | output time 12700800
242 | output time 12787200
243 | output time 12873600
244 | output time 12960000
```

```
245   output time 13046400
246   output time 13132800
247   output time 13219200
248   output time 13305600
249   output time 13392000
250   output time 13478400
251   output time 13564800
252   output time 13651200
253   output time 13737600
254   output time 13824000
255   output time 13910400
256   output time 13996800
257   output time 14083200
258   output time 14169600
259   output time 14256000
260   output time 14342400
261   output time 14428800
262   output time 14515200
263   output time 14601600
264   output time 14688000
265   output time 14774400
266   output time 14860800
267   output time 14947200
268   output time 15033600
269   output time 15120000
270   output time 15206400
271   output time 15292800
272   output time 15379200
273   output time 15465600
274   output time 15552000
275   output time 15638400
276   output time 15724800
277   output time 15811200
278   output time 15897600
279   output time 15984000
280   output time 16070400
281   output time 16156800
282   output time 16243200
283   output time 16329600
284   output time 16416000
285   output time 16502400
```